1   **Spatial and temporal variability of the hydroxyl radical: Understanding the role of**
2   **large-scale climate features and their influence on OH through its dynamical and**
3   **photochemical drivers**

5   Daniel C. Anderson[1,2], Bryan N. Duncan[2], Arlene M. Fiore[3], Colleen B. Baublitz[3], Melanie B.
6   Follette-Cook[2,4], Julie M. Nicely[2,5], Glenn M. Wolfe[2]

8   [1] Universities Space Research Association, GESTAR, Columbia, MD, USA
9   [2] Atmospheric Chemistry and Dynamics Laboratory, NASA Goddard Space Flight Center, Greenbelt,
10   MD
11   [3] Department of Earth and Environmental Sciences, Columbia University, Palisades, NY
12   [4] Morgan State University, GESTAR, Baltimore, MD
13   [5] Earth System Science Interdisciplinary Center, University of Maryland, College Park, College Park,
14   MD

16   *Correspondence to: Daniel C. Anderson (daniel.c.anderson@nasa.gov)*

18   **Abstract**
19   The hydroxyl radical (OH) is the primary atmospheric oxidant, responsible for removing many
20   important trace gases, including methane, from the atmosphere. Although robust relationships
21   between OH drivers and modes of climate variability have been shown, the underlying mechanisms
22   between OH and these climate modes, such as the El Niño Southern Oscillation (ENSO), have not
23   been thoroughly investigated. Here, we use a chemical transport model to perform a 38-year
24   simulation of atmospheric chemistry, in conjunction with satellite observations, to understand the
25   relationship between tropospheric OH and ENSO, Northern Hemispheric modes of variability, the
26   Indian Ocean Dipole, and monsoons. Empirical orthogonal function (EOF) and regression analyses
27   show that ENSO is the dominant mode of global OH variability in the tropospheric column and
28   upper troposphere, responsible for approximately 30% of the total variance in boreal winter.
29   Reductions in OH due to ENSO are centered over the tropical Pacific and Australia and can be as
30   high as 10 - 15% in the tropospheric column. The relationship between ENSO and OH is driven by
31   changes in nitrogen oxides in the upper troposphere and changes in water vapor and O^1D in the
32   lower troposphere. While the spatial scale of the relationship between monsoons, other modes of
33   variability, and OH are much smaller than ENSO, local changes in OH can be significantly larger than
34   those caused by ENSO. These relationships also occur in multiple models that participated in the
35   Chemistry Climate Model Initiative (CCMI), suggesting that the dependence of OH interannual
36   variability on these well-known modes of climate variability is robust. Finally, modeled
37   relationships between ENSO and OH drivers – such as carbon monoxide, water vapor, and lightning
38   – closely agree with satellite observations. The ability of satellite products to capture the
39   relationship between OH drivers and ENSO provides an avenue to an indirect OH observation
40   strategy and new constraints on OH variability.
41

1.0   Introduction
43   The hydroxyl radical (OH), the atmosphere's primary oxidant, removes many trace gases that affect
44   composition and climate. Despite its central role in atmospheric chemistry, the spatiotemporal
45   distributions of OH concentrations are poorly constrained, often confounding interpretation of
46   observed variations and trends of important atmospheric constituents. For example, there are
47   several plausible explanations of the observed fluctuations in the global burden of atmospheric
48   methane (CH_4), the second-most important anthropogenic greenhouse gas. Explanations include
49   variations and trends in both emissions and oxidation of methane (Prather and Holmes, 2017;Rigby

50 et al., 2017;Turner et al., 2017). Better constraints on OH and its dynamical and photochemical
51 drivers are needed to improve confidence in our interpretation of recent methane trends and to
52 project future climate in response to changes in emissions and composition.
53
54 Observational limitations and chemistry climate model disagreement pose challenges to advancing
55 our understanding of the spatiotemporal variability in OH. There are few direct *in situ* OH
56 observations, on local, regional, and global scales (Stone et al., 2012) as OH is both highly reactive,
57 with a lifetime of ~1 s in the free troposphere (Mao et al., 2009), and low in concentration, on the
58 order of 10^6 molecules/cm³. Recent work has demonstrated that a longer-lived intermediate of CH_4
59 oxidation, formaldehyde, shows promise for inferring variability in OH columns over the remote
60 atmosphere (Wolfe et al., 2019). In models of atmospheric chemistry and transport, OH can vary
61 widely, with differences in global methane lifetime, a proxy for OH abundance, between 45 and
62 80% among models in inter-comparison projects (e.g., Voulgarakis et al., 2013;Nicely et al.,
63 2017;Zhao et al., 2019).
64
65 Analysis of the factors causing inter-model differences in the tropospheric OH burden is
66 challenging, as causation is difficult to prove with a species so tightly coupled to a multitude of
67 chemical and meteorological processes. Primary OH production occurs through photolysis of O_3
68 followed by reaction with water vapor ($H_2O_{(v)}$), while secondary production is often regulated by
69 nitrogen oxides ($NO_X = NO + NO_2$) through the reaction of the hydroperoxyl radical (HO_2) with NO.
70 Globally, CO and CH_4 are the primary sinks, although other species, particularly volatile organic
71 compounds (VOCs), can be important regionally. However, attributing OH variability remains
72 challenging, with different models showing widely ranging responses in OH to changes in these
73 drivers, particularly to NO_X and humidity (Wild et al., 2020).
74
75 These chemical and radiative drivers of OH variability are in turn partially regulated by large-scale
76 dynamical features, such as the El Niño Southern Oscillation (ENSO), monsoons, and modes of
77 Northern Hemispheric (NH) variability (*e.g.* the North Atlantic Oscillation (NAO)), through changes
78 in transport and emissions. Oman et al. (2011) and Oman et al. (2013) used satellite observations
79 and chemistry climate models to show that the horizontal and vertical distributions of tropospheric
80 ozone are significantly modulated by ENSO, most prominently through the manifestation of a dipole
81 pattern over southeast Asia and the tropical western Pacific. Sekiya and Sudo (2012) found similar
82 results with the CHASER chemical transport model, along with strong relationships between ozone
83 variability and the Indian Ocean Dipole (IOD), the Arctic Oscillation, and the Asian winter monsoon.
84 ENSO events can also change CH_4 emissions from wetlands (Zhang et al., 2018), CO emissions from
85 biomass burning (Duncan, 2003b;Duncan, 2003a;Rowlinson et al., 2019), and lightning NO
86 production (Murray et al., 2013;Murray et al., 2014;Turner et al., 2018). Relationships between the
87 Madden-Julian Oscillation (MJO) and variability of tropical ozone (Tian et al., 2007;Ziemke et al.,
88 2015), $H_2O_{(v)}$ (Myers and Waliser, 2003), and CO (Wong and Dessler, 2007) have also been shown.
89 Finally, the NAO can alter the long range transport of CO, through increased outflow from Europe
90 over the North Atlantic during its negative phase (Li et al., 2002;Creilson et al., 2003;e.g. Duncan,
91 2004).
92
93 Despite the strong linkages between these dynamical features and OH drivers, there is little
94 research on the relationship between these processes and OH itself. Turner et al. (2018) used a
95 6000-year simulation with free running dynamics to suggest that ENSO is the dominant mode of OH
96 variability at decadal timescales, mainly through its effects on lightning NO emissions. Their study,
97 however, held most forcings and emissions, including greenhouse gas concentrations and biomass
98 burning, to 1860 conditions. Emissions of lightning NO, dust, and dimethyl sulfide were allowed to
99 respond to model meteorology. During the 1997/98 ENSO event, increases in CO from biomass

100   burning led to decreases in OH of 9% on the global scale (Rowlinson et al., 2019) and up to 20%
101   over the Indian Ocean (Duncan, 2003b). Using inversions of observations of methyl chloroform to
102   estimate OH concentrations, Prinn et al. (2001) found OH to be lower during ENSO years,
103   suggesting this could be linked to reduced UV radiation near the surface due to increased cloud
104   coverage. As with ENSO, modeling studies have shown that the Asian monsoon increases OH
105   concentrations in the upper troposphere (UT) through increased lightning NO production, despite
106   increases in convectively lofted OH sinks, particularly CO (Lelieveld et al., 2018).
107
108   Here, we examine how OH and related chemical and radiative factors vary with known modes of
109   climate and atmospheric variability. Using correlation analysis, we compare the relationship
110   between ENSO and tropospheric column OH from the NASA Goddard Earth Observing System
111   (GEOS) Chemistry Climate Model (GEOSCCM) (Strode et al., 2019) and four models that
112   participated in the joint International Global Atmospheric Chemistry (IGAC)/Stratosphere-
113   troposphere Processes And their Role in Climate (SPARC) Chemistry Climate Model Initiative
114   (CCMI) (Morgenstern et al., 2017). After evaluating these relationships from the GEOSCCM model
115   with *in situ* and satellite observations, we explore further the relationship between OH, its
116   precursors, and ENSO. Finally, we expand the analysis to include not only ENSO but also other
117   modes of internal climate variability.
118
119   **2.0   Methods**
120   In this section, we outline the methodology used to understand the relationship between OH and
121   large-scale dynamical drivers. First, we describe the analysis methods used in Section 2.1. In
122   Sections 2.2 and 2.3, we describe the relevant details of the GEOSCCM and CCMI simulations,
123   respectively.
124
125   **2.1   Description of Analysis Methods**
126   Because the factors driving OH concentrations and interannual variability are altitude dependent,
127   we divide the atmosphere into 4 layers: the surface to the top of the PBL (PBL), from the top of the
128   PBL to 500 hPa (Lower Free Troposphere: LFT), between 500 and 300 hPa (Middle Free
129   Troposphere: MFT), and from 300 hPa to the tropopause (Upper Free Troposphere: UFT). Output
130   from each model has been vertically averaged to these layers on a seasonal basis. In addition, we
131   also examine the tropospheric column.
132
133   To help determine the relationship between the modes of climate variability and photochemical
134   and meteorological variables archived by the various models, we regress model output against
135   different climate indices. To perform the regression, we first detrend the output on a monthly basis
136   and then regress the model variable against a specific climate index (*e.g.* ENSO index) for 1980 to
137   2018. We perform these regressions on each grid cell for each of the 4 layers as well as for the
138   tropospheric column. In the results below, we only include regressions where the Pearson
139   correlation coefficient (r) exceeds 0.5, unless otherwise indicated. Using other methods to define
140   significance of a regression, such as a two-tailed student t test with p values less than 0.05, does not
141   significantly alter the results.
142
143   Climate features considered here include ENSO, the IOD, several Northern Hemispheric
144   atmospheric modes of variability, and various monsoons. We use the ENSO multivariate index
145   (MEI) (Wolter and Timlin, 2011) and the Dipole Mode Index (DMI) for the Indian Ocean Dipole,
146   obtained from https://psl.noaa.gov/enso/mei/ and
147   https://psl.noaa.gov/gcos_wgsp/Timeseries/DMI/, respectively. Northern Hemispheric modes
148   considered are the NAO, the East Atlantic Pattern (EA), the Pacific North American Pattern (PNA),

149   the East Atlantic Western Russian Pattern, the Scandinavian Pattern, the West Pacific Pattern, the
150   East Pacific North Pacific Pattern, and the Tropical Northern Hemisphere Pattern. Indices for the
151   NH modes were taken from the NOAA Climate Prediction Center (available online at
152   https://www.cpc.ncep.noaa.gov/data/teledoc/telecontents.shtml) and were determined from a
153   rotated principal component analysis of the 500 hPa geopotential height of the National Center for
154   Environmental Prediction Reanalysis. Monsoons included in this analysis are the Indian, South
155   American, North American, South African, North African, Australian, and the Western North Pacific.
156   We calculate the monsoon index for each model used in this study based on the definitions of Yim et
157   al. (2013), where the index is defined by the difference of zonal winds at 850 hPa between two,
158   monsoon-specific regions. See Table 2 in Yim et al. (2013) for more details. Because the GEOSCCM
159   (Section 2.2) and CCMI models (Section 2.3) included here are constrained or nudged to different
160   reanalyses (MERRA, MERRA2, JRA-55, and the ERA-interim), the calculated monsoon index varies
161   among the models, although the indices of a given monsoon from each model are highly correlated
162   with one another (generally $r^2 > 0.9$).

164   In addition to regression analysis, we also performed an empirical orthogonal function (EOF)
165   analysis for tropospheric column OH (TCOH) and separately for each of the four layers described
166   above. EOF analysis allows for the statistical determination of the spatial modes of OH variability
167   and their variation with time without *a priori* knowledge of the controlling mechanisms (e.g.,
168   Barnston and Livezey, 1987). To perform the analysis, OH fields for each grid box were detrended
169   by subtracting a linear fit and standardized with the standard deviation before calculating the EOF.
170   We report here only the first and second EOFs and their associated principal component time series
171   as none of the other EOFs correlated spatially or temporally with any of the modes of climate
172   variability discussed here.

2.2   MERRA-2 GMI Simulation Description
175   To understand the interannual variability of OH, we use the MERRA-2 GMI (Modern-Era
176   Retrospective analysis for Research and Applications Global Modeling Initiative) simulation,
177   publicly available at https://acd-ext.gsfc.nasa.gov/Projects/GEOSCCM/MERRA2GMI/. This is a run
178   of the GEOSCCM model (Strode et al., 2019) constrained to meteorology from MERRA-2 (Gelaro et
179   al., 2017) that uses the GMI chemical mechanism (Duncan et al., 2007;Oman et al., 2013;Gelaro et
180   al., 2017). The GMI chemical mechanism includes approximately 120 species and 400 reactions,
181   characterizing the photochemistry of the troposphere and stratosphere. The model was run from
182   1980 to 2018 at a resolution of c180 on the cubed sphere, equivalent to approximately 0.625°
183   longitude × 0.5° latitude, with 72 vertical levels. The model was run in a replay mode (Orbe et al.,
184   2017) and constrained to temperature, pressure, and winds from MERRA-2. Model output is
185   available at daily and monthly resolutions, with hourly output available only for some local satellite
186   overpass times. All data used in this work is monthly averaged unless otherwise indicated.

188   Anthropogenic emissions are from the Measuring Atmospheric Composition and Climate mega City
189   (MACCity) inventory (Granier et al., 2011) for 1980 – 2010, and then from the Representative
190   Concentration Pathway 8.5 (RCP8.5) scenario for 2011 – 2018. Biomass burning emissions are
191   from the Global Fire Emissions Database (GFED) 4s inventory starting in 1997 (Giglio et al., 2013).
192   Biomass burning emissions from before 1997 are calculated from scale factors derived from
193   aerosol index data from the Total Ozone Mapping Spectrometer (TOMS) instrument, as described in
194   Duncan (2003). Biogenic emissions are calculated online using the Model of Emissions of Gases and
195   Aerosols from Nature (MEGAN) model (Guenther et al., 1999;Guenther et al., 2000). A known high
196   bias in isoprene emissions from MEGAN (e.g., Wang et al., 2017), could exacerbate low modeled OH
197   in regions dominated by biogenic VOC emissions. Lightning NO emissions are based on the
198   cumulative mass flux (Allen et al., 2010), with constraints from the Lightning Imaging Sounder

199 (LIS)/Optical Transient Detector (OTD) v2.3 climatology (Cecil et al., 2014). Total, global lightning
200 NO emissions are scaled to be 6.5 Tg N/year for each year of the simulation, although emissions
201 demonstrate significant interannual variability on the local scale. For example, over the tropical
202 Pacific, an area we will investigate throughout this paper, peak emissions are 1.5 times higher than
203 minimum emissions over the time period studied here (Fig. S1). Methane concentrations are
204 specified as latitude- and time-dependent boundary conditions.
205
206 **2.3 IGAC/SPARC Chemistry Climate Model Initiative (CCMI) Phase 1 Model Simulations**
207 To place the results from MERRA2 GMI in the context of other models, we compare our simulation
208 with those from CCMI. The CCMI was conducted to help assess the ability of a suite of models to
209 address various aspects of atmospheric chemistry, including trends in tropospheric ozone and the
210 controlling mechanisms of OH (Morgenstern et al., 2017). Output from these models have already
211 been used to assess various aspects of tropospheric OH (Zhao et al., 2019;Nicely et al., 2020), HCHO
212 (Anderson et al., 2017), O_3 (Revell et al., 2018;Dhomse et al., 2018) and meteorological variables
213 (Orbe et al., 2020). Modeling groups conducted multiple runs, including a forecast scenario to 2100
214 and two hindcast scenarios, one with free-running meteorology and one, the specified dynamics
215 (SD) scenario, in which models were either nudged to meteorological reanalyses or run as chemical
216 transport models (Orbe et al., 2020).
217
218 We perform a similar analysis as with MERRA2 GMI with four models that performed the CCMI SD
219 run. We use the SD run, which spanned the years 1980 – 2010, instead of the other scenarios to
220 allow for more direct comparison among the CCMI models as well as with MERRA2 GMI and
221 observations from satellite. We include only models that output data for all years between 1980
222 and 2010 and that have non-methane hydrocarbon chemistry in their chemical mechanisms.
223 Models used here are WACCM (Solomon et al., 2015), CHASER (MIROC-ESM) (Watanabe et al.,
224 2011), a setup of EMAC with 90 vertical levels (EMAC) (Jöckel et al., 2016), and MRI-ESM1r1
225 (Yukimoto et al., 2012). We omit CAM4Chem and a different setup of EMAC with 47 vertical levels
226 because results for those models are essentially identical to WACCM and EMAC90, respectively.
227 EMAC90 and CHASER were nudged to the ERA-interim reanalysis, WACCM to the MERRA
228 reanalysis, and MRI to the JRA-55 reanalysis. Sea surface temperatures (SST) and sea ice were
229 prescribed in each model with the Hadley SST dataset. Anthropogenic emissions were from the
230 MACCity inventory, while lightning NO_X was calculated online using model-specific
231 parameterizations. Further model details can be found in Orbe et al. (2020), Morgenstern et al.
232 (2017), and references therein.
233
234 As with the MERRA2 GMI analysis, we use monthly averaged output. For layer averaging, only
235 EMAC90, WACCM, and MRI output a tropopause height, while no models output PBL height. To
236 calculate the tropopause height for CHASER, we used the relationship between O_3 and CO as
237 described in Pan et al. (2004). PBL height for all models was determined from the bulk Richardson
238 number (Seibert et al., 2000).
239
240 **3.0 MERRA2 GMI Simulation Evaluation**
241 While there has been some evaluation of the MERRA2 GMI simulation (Ziemke et al., 2019;Strode et
242 al., 2019), species in the simulation relevant to this study have not been investigated. As a result,
243 we evaluate MERRA2 GMI using *in situ* observations of OH and related species as well as remotely
244 sensed observations of OH drivers in order to understand the effect any model biases could have on
245 our results. In Section 3.1, we use *in situ* observations from the first two deployments of the
246 Atmospheric Tomography (ATom) campaign to evaluate OH, CO, and HCHO over the remote Pacific

247   and Atlantic Oceans. In Section 3.2, we also compare output to satellite observations of CO, $H_2O_{(v)}$,
248   and NO_2 to evaluate the model over larger temporal and spatial scales.

249

3.1   Evaluation of MERRA2 GMI with *in situ* Observations

251   During the ATom campaign, a suite of air quality and climate relevant trace gases and aerosols were
252   measured throughout the remote Pacific and Atlantic. During each of the deployments, aircraft
253   transected the Pacific from Alaska to New Zealand, went around Tierra del Fuego, and travelled
254   north over the Atlantic to Greenland. Each flight consisted of a series of ascents and descents
255   allowing for vertical profiling across most latitudes of the remote Pacific and Atlantic Oceans. The
256   combination of the flight track and the repetition across seasons provided unprecedented sampling
257   of many trace gases, including OH. As part of the ATom campaign, a limited subset of species,
258   including OH and CO, from the MERRA2 GMI simulation were output hourly for the duration of
259   ATom1 (July – August 2016) and ATom2 (January – February 2017) only, allowing for direct
260   comparison to the *in situ* observations. Only daily or longer resolution output is available for the
261   other deployments, and, as a result, we focus our analysis on these first two deployments.

262
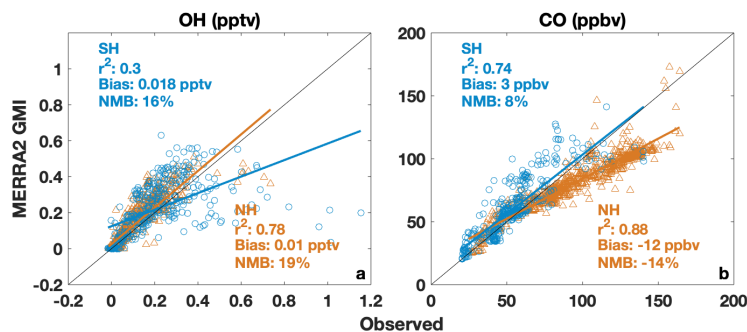
Figure 1: Regression of observed OH (a) and CO (b) from ATom 2 (boreal winter 2017) against hourly output from MERRA2 GMI interpolated to the ATom flight track. Data from the Southern (blue circles) and Northern (orange triangles) Hemisphere are shown, along with the r^2, bias, and normalized mean bias (NMB) for each hemisphere. Observations and model output have been filtered for biomass burning influence.

268   Observations used here include OH (Brune et al., 2020) and CO (Santoni et al., 2014), with 2σ
269   uncertainties of 35% and 3.5 ppbv, respectively. Data have been averaged to a 5-minute time base
270   and filtered for biomass burning influence, defined as times when concentrations of HCN and CO
271   are both above the 75th percentile for the individual ATom deployments. We omit the biomass
272   burning influenced parcels because small differences in measured and modeled winds could result
273   in misplacement of modeled biomass burning plumes, resulting in unrealistically large differences
274   in OH. Inclusion of the biomass burning influenced parcels does not significantly change the model
275   bias but does degrade the the correlation. For comparison of the observations to MERRA2 GMI,
276   hourly data were output by the model and then bilinearly interpolated in the horizontal and
277   linearly interpolated in time and in the vertical to the *in situ* observation time and location.

278

279   MERRA2 GMI has a OH high bias of approximately 20% (Fig. 1) when compared to observations
280   from ATom 2. A regression of measured and modeled OH shows moderate to high correlation in
281   both the Southern Hemisphere (SH) and NH, with r^2 values of 0.30 and 0.78, respectively.
282   Normalized Mean Biases (NMB) relative to the observations are similar in both the NH (19%) and
283   SH (16%), with nearly identical high biases during the summer deployment of ATom1 (Fig. S2).
284   The comparatively poorer model performance for OH in the SH is being driven by continental

285   outflow from South America and New Zealand. When data from these regions are omitted, the
286   correlation for the SH increases to 0.63 and the NMB is 22%.
287
288   Agreement between observed and modeled CO shows a strong hemispheric dependence, with an
289   NMB of -14% in the NH (i.e., the model is lower than observations by 14%) and 8% in the SH,
290   although both hemispheres have a strong correlation ($r^2 > 0.7$). While agreement in the SH
291   improves in the summer, with an NMB of 2% (Fig. S2), the model underestimate in the NH is even
292   more pronounced (NMB = -20%). This NH low bias in CO is consistent with the overestimate in OH
293   and is a well-known problem in global chemistry models (Naik et al., 2013;e.g. Stein et al., 2014).
294
295   Comparison of the MERRA2 GMI simulation to *in situ* observations demonstrates that the model
296   captures the spatial variability of OH and its predominant global sink, CO, in the remote atmosphere
297   during both the NH summer and winter, with the exception of OH off the coast of South America
298   and New Zealand. The poorer agreement between measured and modeled OH in regions of fresh,
299   continental outflow suggests that modeled relationships between climate modes and OH in these
300   regions might be more uncertain than in the remote atmosphere.
301
302   **3.2   Evaluation of MERRA2 GMI with Satellite Observations**
303   While there are no remotely sensed observations of tropospheric column OH (TCOH), there are
304   satellite observations of OH drivers. Comparing these observations to MERRA2 GMI allows for
305   model evaluation over larger spatial and temporal scales than with ATom. Satellite data used here
306   include tropospheric CO columns from the Measurement Of Pollutants In The Troposphere
307   (MOPITT) instrument, $H_2O_{(v)}$ from the Atmospheric Infrared Sounder (AIRS), and tropospheric NO_2
308   from the Ozone Monitoring Instrument (OMI). AIRS is on the Aqua satellite, with a daily, local
309   overpass time of approximately 13:30. We use the monthly averaged, Level 3, Version 6 standard
310   physical retrieval (Susskind et al., 2014) from 2003 to 2018. For MOPITT CO on the Terra satellite,
311   we use the Level 3, V008 retrieval that uses both near and thermal infrared radiances (Deeter et al.,
312   2019) from 2001 to 2018. MOPITT has a daily, local overpass time of approximately 10:30. Both
313   satellite products have a global horizontal resolution of 1° × 1°. We also use the OMI NO_2 Version 3,
314   Level 3 product (Krotkov et al., 2017) from 2005 to 2018. Data have been regridded to 1° × 1°
315   horizontal resolution. OMI is located on the Aura satellite and, as with AIRS, has a local overpass
316   time of approximately 13:30. For comparison of the satellite retrievals to MERRA2 GMI, we use
317   monthly fields of the model variables output at the satellite overpass time.
318
319   When compared to MOPITT in boreal winter, tropospheric column CO from MERRA2 GMI (Fig. 2,
320   first column) shows similar results to that found through comparison to the *in situ* observations,
321   namely a low bias in the NH (9%) and high bias in the SH (7%). Differences over the tropical
322   Pacific, an area that will be shown later to have a strong relationship between ENSO and OH, are
323   generally less than 10%, while a noticeable high bias exists over parts of South America. Results for
324   June – August (JJA) are spatially similar (Fig. S3), with a NH low bias of 20% and overestimates of
325   column CO, averaging 45%, in the SH corresponding with areas of biomass burning.
326
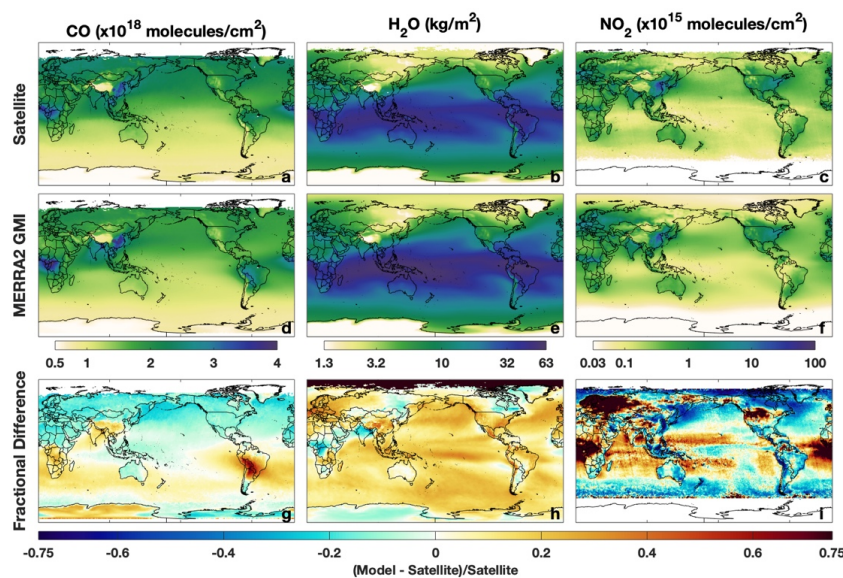
Figure 2: Tropospheric column CO (left), $H_2O_{(v)}$ (middle), and NO_2 (right) from MOPITT, AIRS, and OMI, respectively (top row), and MERRA2 GMI (middle row) averaged over the satellite lifetime for DJF. The fractional difference between MERRA2 GMI and the satellite is shown in the bottom row.

MERRA2 GMI captures the spatial distribution of $H_2O_{(v)}$, although the model is biased high in both the column and throughout much of the troposphere. Overestimates in column $H_2O_{(v)}$ are ~14% in both December – February (DJF) (Fig. 2h) and JJA (Fig. S3). These overestimates extend over most of the world's oceans, and only small regions over northern India, central Africa, eastern Russia, and eastern Canada show any underestimate in $H_2O_{(v)}$. Fractional differences in $H_2O_{(v)}$ between MERRA2 GMI and the different AIRS pressure levels are most pronounced in the tropical UT (Fig. 3). At pressures greater than 700 hPa, modeled $H_2O_{(v)}$ is generally within 10% of the observations, while for pressures less than 500 hPa, modeled $H_2O_{(v)}$ in the equatorial region disagrees with observations by 55% on average.

Agreement between observed and modeled NO_2 is weaker than for the other species examined here. While MERRA2 GMI appears to capture the regions with local NO_2 maxima – notably those over central Africa, eastern China, and the northeastern United States – the magnitudes frequently differ. The simulation shows a significant high bias over central Africa and the equatorial Atlantic on the order of 100%, suggesting that biomass burning emissions of NO_X, the dominant NO source in this region, are too high, consistent with the CO comparison to MOPITT. In contrast, concentrations over eastern Asia are too low in the model, suggesting errors in the anthropogenic emissions inventory and/or in the NO_X lifetime. Strode et al. (2019) also evaluated NO_2 in MERRA2 GMI, comparing trends in tropospheric column NO_2 over the eastern US and eastern China in MERRA2 GMI and OMI. They found that although trends were similar between the simulation and observations in both regions, the magnitude of the trends differed, likely due to errors in the MACCity emissions inventory.
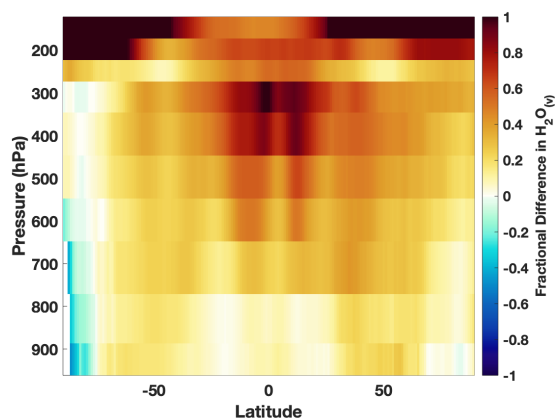
354
355   *Figure 3: The fractional difference in zonal mean $H_2O_{(v)}$ between MERRA2 GMI and AIRS for the different AIRS pressure layers for*
356   *DJF. Positive numbers indicate a high bias in the model.*

357   As with the *in situ* observations, comparison between MERRA2 GMI and satellite retrievals
358   demonstrates that the simulation is able to capture the distribution of the chemical drivers of OH in
359   remote regions, which tend to exhibit the strongest relationship between OH and climate modes
360   (see Section 4.0). These results lend confidence to the analysis described in Sections 4.0 and 5.0
361   and suggest the findings in remote regions are likely applicable to the actual atmosphere. The large
362   disagreement between the simulation and observed column CO and NO_2 in regions that are
363   significantly impacted by biomass burning emissions suggests, however, that modeled relationships
364   of chemical species with modes of climate variability in these regions should be viewed with
365   caution. We further evaluate the ability of the simulation to capture the relationship between ENSO
366   and CO, $H_2O_{(v)}$, and NO_2 using satellite observations in Section 5.1.2.
367
368   **4.0   The Relationship between Simulated OH Variability and Climate Modes**
369   When considered in concert, the modes of climate variability evaluated here (i.e., ENSO, the IOD,
370   and NH modes) along with monsoons explain a substantial fraction of the simulated tropospheric
371   OH interannual variability over 19 – 40% of the global atmosphere by mass, depending on season.
372   Figure 4 highlights regions that show significant correlation between TCOH and the NH modes
373   (purple), monsoons (light blue), ENSO (green), and the IOD (orange) for each season in MERRA2
374   GMI output. In all seasons, correlation with ENSO has the largest spatial extent, but in DJF and
375   MAM, for example, the 8 NH modes can explain TCOH variability over large swaths of the NH,
376   comprising 10% of the globe. In JJA, the climate modes have the smallest spatial coverage (19% of
377   the globe), while the IOD, consistent with its seasonal variability, only has a widespread correlation
378   with TCOH during SON. Similar patterns are found for the individual layers (Fig. S4).
379
380   Below, we examine the relationships between tropospheric OH and the various modes of climate
381   variability demonstrated in Figure 4. First, in Section 5.0, we show that El Niño events lead to
382   global reductions in tropospheric OH, with changes being driven by increased primary production
383   in the PBL and decreased secondary production in the UFT. In Section 6.0, we demonstrate that the
384   effects on OH from NH modes of variability, the IOD, and some monsoons have limited spatial
385   scales, as compared to ENSO, but can significantly alter local OH distributions. In both sections, we
386   also compare simulations from MERRA2 GMI to simulations from the CCMI, demonstrating that the
387   relationship between OH and climate modes is robust among multiple models.
388
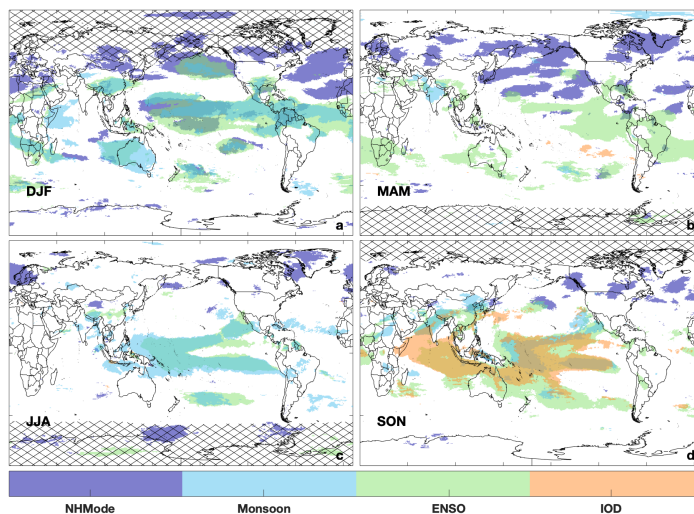
389
390 *Figure 4: Regions that show a significant correlation (absolute value of r >0.5) between a NH mode (purple), monsoon (light*
391 *blue), ENSO (green), or IOD (orange) and TCOH for each season. Regions with TCOH less than 1 x 10^{11} molecules/cm^2 have been*
392 *hatched out.*

393 **5.0 Relationship between Simulated OH Variability and ENSO in MERRA2 GMI**
394 To understand the relationship between OH, its drivers, and ENSO, we first investigate the OH
395 production rate. In the MERRA2 GMI simulation, the OH production rate is primarily dependent on
396 reactions 1 – 4, where O^{1}D is produced from the photolysis of tropospheric O$_3$. In the free
397 troposphere, these four reactions comprise at least 95% of OH production in the tropics, on
398 average, and at least 90% in the PBL. Only in the regions with large biogenic emissions (e.g., South
399 America and central Africa) do other reactions contribute more than 15% of the total OH
400 production in the PBL. As will be shown, the effects of ENSO on OH are primarily focused away
401 from these regions, so we restrict our analysis to reactions 1-4.
402

$$H_2O_2 + h\upsilon \rightarrow 2OH \qquad \qquad \text{(Reaction 1)}$$
$$NO + HO_2 \rightarrow NO_2 + OH \qquad \qquad \text{(Reaction 2)}$$
$$O_3 + HO_2 \rightarrow 2O_2 + OH \qquad \qquad \text{(Reaction 3)}$$
$$H_2O + O^1D \rightarrow 2OH \qquad \qquad \text{(Reaction 4)}$$

403
404 During El Niño events, the dominance of these individual reactions in producing OH varies with
405 altitude. Figure 5 shows the zonal mean of the fraction of total OH production from the H$_2$O + O^{1}D
406 (a) and NO + HO$_2$ (b) reactions as well as the total OH production rate (c) during El Niño events in
407 DJF. We focus our analysis on DJF throughout Section 5.0 because that is the season with the
408 largest impact of ENSO on OH as shown in Figure 4. The relative importance of the individual
409 reactions is similar during neutral and La Niña years (not shown) and is in agreement with
410 previous model studies (e.g. Spivakovsky et al., 2000). The H$_2$O + O^{1}D reaction is dominant from the
411 surface to about 800 hPa through much of the SH and the tropics, while, near the surface, the NO +
412 HO$_2$ reaction only has large impacts in the NH mid-latitudes. This influence of NO$_X$ in the NH mid-
413 latitudes extends through much of the troposphere. In the UFT, this reaction is the greatest
414 contributor to total OH production at all latitudes except the NH polar region, where the HO$_2$ + O$_3$
415 reaction dominates during polar night (Fig. S5). Total OH production in the polar regions, however,
416 is orders of magnitude lower than in the tropics. Outside of the polar regions, the HO$_2$ + O$_3$ and
417 H$_2$O$_2$ photolysis reactions generally contribute between 10 and 30% of the total rate (Fig. S5).

418 Because of the differing importance of the individual OH production reactions with altitude, we
419 examine the relationship between OH and ENSO separately for each of the atmospheric layers and
420 for TCOH.
421
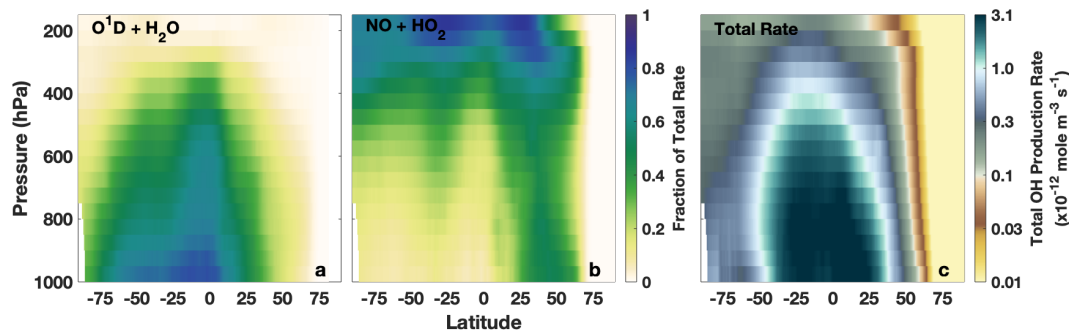
422
423 *Figure 5: Zonal mean of the fractional contribution of the $O^1D + H_2O$ (a) and $NO + HO_2$ (b) reactions to the total OH production*
424 *rate as well as the total OH production rate (c) for El Niño events (MEI > 0.5) for DJF averaged over 1980-2018.*

425 **5.1.1   Tropospheric Column OH**
426 **5.1.1   The Relationship between Simulated TCOH and ENSO**
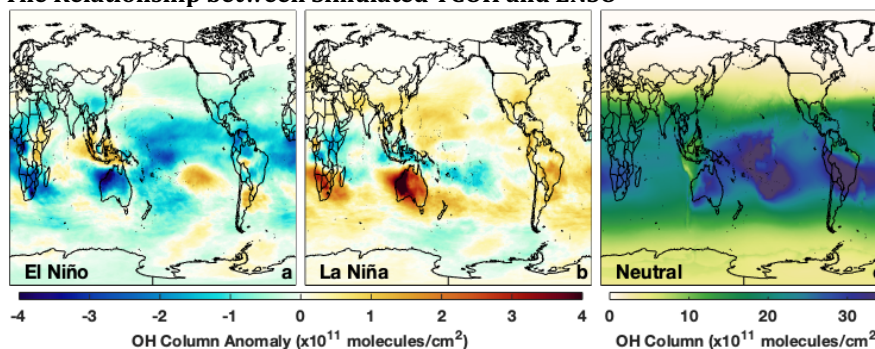
427
428 *Figure 6: Absolute difference in TCOH between El Niño events and neutral years (a) for DJF averaged over 1980 – 2018. El*
429 *Niño events are defined as having a MEI value greater than 0.5, and neutral years have a MEI value between -0.5 and 05.*
430 *The analogous plot for La Niña events (MEI less than -0.5) is also shown (b). Panel c shows the average OH column for neutral*
431 *years.   The 1980 – 2018 time period includes 11 El Niños, 12 La Niñas, and 15 neutral years.*

432 As shown in Figure 6, TCOH decreases by 3.3% during El Niño events (relative to neutral events)
433 equatorward of 30° in DJF and is characterized by widespread decreases in the tropics and
434 subtropics, especially northern Australia, and west-central and southern Africa. Regional increases
435 are found over eastern Africa, the east-central Pacific, southern South America, and Indonesia.
436 Maximum decreases in TCOH are on the order of 4.5×10^{11} molecules/cm^2 ($\sim$10-15%) and are
437 centered over northern Australia, while maximum increases in TCOH ($\sim$2.5$\times 10^{11}$ molecules/cm^2)
438 are centered over Sumatra.
439
440 During La Niña events, TCOH increases relative to neutral years over much of the globe, although
441 the changes are not necessarily symmetric with those seen during El Niño events. Increases over
442 Australia are on the order of 1 to 2×10^{11} molecules/cm^2, on par with the decreases seen during El
443 Niño, but the changes during La Niña are centered over Western Australia and the Indian Ocean.
444 Over the Pacific, the magnitude of the OH increase is lower (on the order of 0.5 to 1×10^{11}
445 molecules/cm^2) than the decreases found during El Niño, and some regions off the coast of Hawaii

446   and Papua New Guinea show decreases during both ENSO phases. Besides these two regions, there
447   are also significant decreases in OH over eastern Africa and in the southern portion of South
448   America.
449
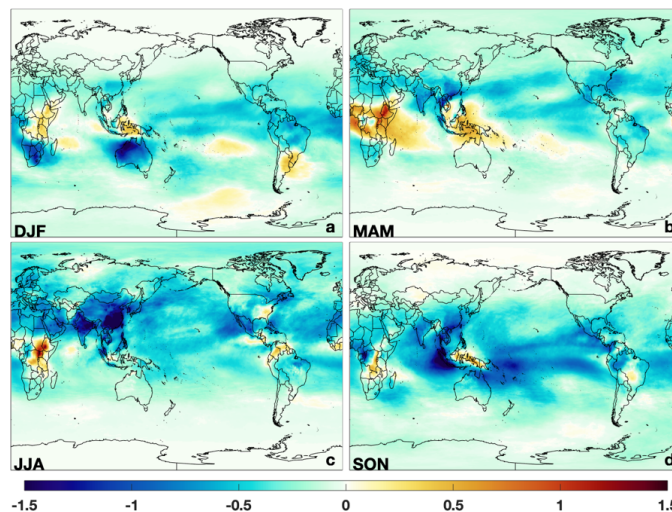
451   Figure 7: The first EOF of TCOH from MERRA2 GMI for DJF (a), MAM (b), JJA (c), and SON (d).

452   Consistent with these widespread changes in TCOH, EOF analysis demonstrates that over most
453   seasons, JJA being the notable exception, ENSO is the dominant mode of OH variability. Figure 7
454   shows the spatial component of the first EOF of TCOH for the four seasons. While EOF analysis does
455   not quantify changes in column content, it does highlight, for each mode of variability, regions
456   where changes in TCOH are most prominent. For DJF, the first EOF (Fig. 7a) is almost identical to
457   the composite figure showing OH anomalies during El Niño (Fig. 6a). Likewise, the temporal
458   component of the 1st EOF strongly correlates with the MEI (r^2 = 0.70, Table 1). In DJF, the first EOF
459   is responsible for 29% of the total variance for TCOH. Although ENSO is the dominant mode,
460   however, 70% of the variability is still unexplained.
461
462   While the spatial pattern of the EOF varies seasonally (Fig. 7), ENSO shows similar levels of
463   correlation to the temporal component of the 1st EOF in MAM and SON as for DJF, with r^2 values of
464   0.54 and 0.60, respectively. For MAM, again the EOF shows regions with a negative sign over much
465   of the Northern Hemisphere, with the largest magnitude centered over the Pacific Ocean, India, and
466   Atlantic coast of the United States. Regions with an opposite sign include the Maritime Continent
467   and much of central Africa. In SON, almost all of the tropics show some response, with major
468   centers off the east coast of Papua New Guinea and off the west coast of Sumatra. In addition, there
469   is a larger response over the Indian Ocean than for other months, also evident in the regression of
470   TCOH with the MEI, suggesting the possible influence of the IOD, which is correlated with ENSO (r^2
471   = 0.30). This seasonal component in the strength of the relationship between the EOF and the MEI
472   is also reflected in the correlation analysis (Fig. 4), where the area of correlation between TCOH and
473   the MEI maximizes in DJF and minimizes in JJA.
474
475   *Table 1: For each season, we show the r^2 of the correlation of the temporal component of the EOF that has the highest*
476   *correlation with the MEI for TCOH and for OH in each layer. In addition, we also indicate the percent of the total variance*

477 *explained by that EOF. With the exception of the values indicated by a *, the 1st EOF has the highest correlation with the MEI.*
478 *Those indicated with a * are the 2nd EOF.*

Month	Column		UFT		MFT		LFT		PBL	
	Pct. Variance	r^2	Pct. Variance	r^2	Pct. Variance	r^2	Pct. Variance	r^2	Pct. Variance	r^2
DJF	29.4	0.7	37.6	0.73	20.8	0.81	11.7*	0.55	12*	0.85
MAM	25.9	0.54	36.2	0.61	23.4	0.40	9.5*	0.48	9.3*	0.59
JJA	30.7	0.25	44.6	0.14	29	0.15	27.7	0.06	39.4	0.07
SON	33.2	0.60	41.1	0.50	22.8	0.63	12.3*	0.59	9.3*	0.63

479
480 **5.1.2 The Relationship between TCOH Drivers and ENSO**
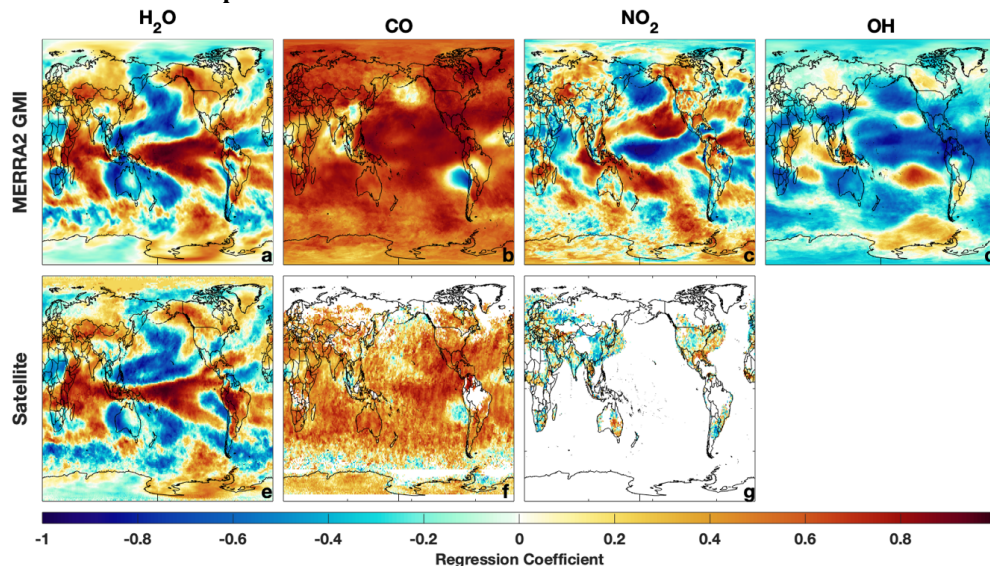
481
482 *Figure 8: Regression of tropospheric column $H_2O_{(v)}$ (a), CO (b), NO_2 (c), and OH (d) from MERRA2 GMI (top) and satellite retrievals*
483 *from AIRS (e), MOPITT (f), and OMI (g) against the MEI for DJF over the satellite lifetime. OMI NO_2 includes only grid boxes with*
484 *greater than the averaged noise in the tropospheric column retrieval (5×10^{14} molecules/cm²) for more than 6 years of the time*
485 *series.*

486 To understand the factors driving ENSO-related changes in TCOH, we also investigate the
487 relationship between OH precursors and ENSO. Figure 5 demonstrates that the $O^1D + H_2O$ and $NO +$
488 HO_2 reactions control zonal mean OH production in the tropics. As a result, we investigate the
489 relationship between tropospheric column $H_2O_{(v)}$, CO, NO_2 and ENSO using both MERRA2 GMI
490 output and satellite retrievals. We use NO_2 here, instead of NO, because of its observability from
491 space, although simulated NO demonstrates similar spatial correlation patterns with the MEI as
492 simulated NO_2.
493
494 Regression of total column $H_2O_{(v)}$ from AIRS against the MEI (Fig. 8e) reveals a tri-pole pattern over
495 the Pacific Ocean, with an area of positive correlation throughout much of the equatorial Pacific
496 Ocean and areas of anti-correlation poleward of this region, in agreement with previous work (e.g.
497 Shi et al., 2018). Each of these areas is well-captured by the MERRA2 GMI simulation (Fig. 8a),
498 showing nearly identical spatial patterns and strength of correlation over most of the globe. This
499 relationship between $H_2O_{(v)}$ and ENSO can be explained by the increased convective uplifting in the
500 equatorial Pacific and associated increased subsidence poleward of this region during El Niño

501 events. While the anticorrelation between $H_2O_{(v)}$ and the MEI over Australia and southern Africa
502 are consistent with the decrease in TCOH over these regions during El Niño events (Fig. 6), the
503 positive correlation between $H_2O_{(v)}$ and the MEI over the equatorial Pacific suggests there must be
504 competing effects from other OH drivers in order to explain the decreases in TCOH in this region.
505
506 Simulated tropospheric column NO_2 is strongly anti-correlated with ENSO over the equatorial
507 Pacific, indicating a suppression of OH production when the MEI is positive (El Niño), consistent
508 with Figure 6. Column NO_2 exhibits the opposite correlation pattern as $H_2O_{(v)}$ over the Pacific, with
509 decreases in NO_2 in regions with increased $H_2O_{(v)}$ and vice versa. The similarities in the spatial
510 correlation patterns for NO_2 and $H_2O_{(v)}$ with the MEI suggests that convection is also at least
511 partially driving the changes in NO_2 in the equatorial Pacific. Changes in the Walker Circulation
512 associated with El Niño events have been shown to redistribute O_3 in the tropics, resulting in a
513 dipole pattern over the western and central Pacific (Oman et al., 2011). Analysis of vertical winds
514 and the NO_2 anomaly (Fig. S6) suggest a similar mechanism for NO_2. OMI data are insufficient to
515 evaluate the simulated relationship between ENSO and column NO_2 based on our criteria of filtering
516 data below the monthly averaged noise in the NO_2 retrieval.
517
518 The dominant OH sink throughout the troposphere is CO, which is responsible for 50% or greater of
519 OH loss at all tropospheric pressures and latitudes (Fig. S7) during El Niño events. Tropospheric
520 column CO and the MEI are positively correlated over most of the globe in both MERRA2 GMI and in
521 MOPITT (Figs. 8b and f, respectively), suggesting strong increases in CO during El Niño events. This
522 increase in CO is associated with increased biomass burning, particularly in Indonesia, and is
523 consistent with the modeled decrease in OH (e.g. Duncan, 2003b) and with the widespread
524 decrease in TCOH over much of the tropics.
525
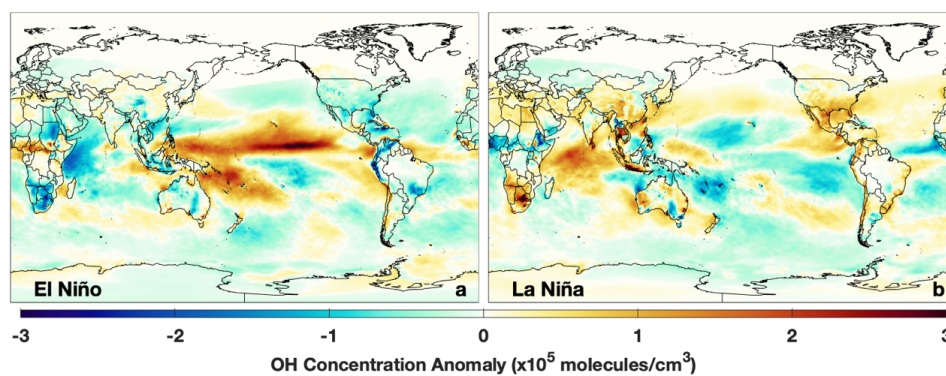
526
527 *Figure 9: Same as Figure 6 except for the PBL level.*

528 **5.2   The Planetary Boundary Layer**
529 **5.2.1 The Relationship between PBL OH and ENSO**
530 In contrast to the tropospheric column (Fig. 6), OH in the PBL increases by 3% equatorward of 30°
531 during El Niño events (Fig. 9), although the geographic extent of these changes is more limited than
532 for TCOH. PBL OH exhibits an area of strong positive correlation with the MEI (Fig. 10d) over the
533 central Pacific, marked by increases in concentrations on the order of 2-3 × 10^5 molecules/cm³,
534 approximately 15% higher than concentrations in neutral years. Changes in the PBL during La Niña
535 are smaller, with concentrations only decreasing about 5 – 10% over the tropical Pacific. Regions
536 with significant correlation between PBL OH and the MEI are distinctly smaller than in the UFT (Fig.
537 10) and for TCOH (Fig. 4a), further emphasizing the comparatively limited spatial effects of ENSO in
538 the PBL.

539
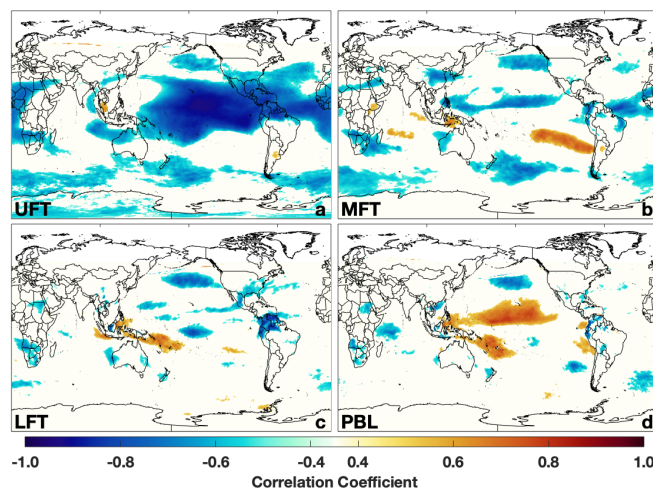
540
541
Figure 10: Correlation of OH from MERRA2 GMI with the MEI for the different atmospheric layers in DJF.

542 The more geographically limited changes in OH shown by the composite and regression analyses
543 are consistent with EOF analysis. During all seasons except JJA, ENSO correlates more strongly with
544 the 2nd EOF for the PBL (Table 1), suggesting another mechanism is the dominant mode of
545 variability. In general, the r^2 with ENSO is 0.5 or higher and the mode contributes approximately
546 10% of the total variance. In contrast to the ENSO related EOFs, the first EOF (Fig. S8) for the DJF
547 PBL layer reveals a spatial pattern much more limited to continental regions and areas of
548 continental outflow, suggesting that this mode of variability is potentially reflective of long-term
549 emission trends, in both anthropogenic and biomass burning emissions. This is more evident in the
550 1st EOF for JJA, where the spatial pattern shows opposite signs over regions with known net
551 emissions reductions (the United States, Europe, and Japan) and those with known net emissions
552 increases (China, India, the Middle East) over the 1980 – 2018 period examined here.
553

554 **5.2.2 The Relationship between PBL OH drivers and ENSO**
555 Approximately 80% of the zonal mean OH production in the tropical PBL during El Niño events is
556 from the $H_2O + O^1D$ reaction (Fig. 5a), suggesting that changes in these two species are driving the
557 interannual variability of OH in the PBL. Figure 11 shows the correlation between OH production
558 from this reaction as well as the total OH production rate against the MEI for the PBL. Similar plots
559 for the other OH production reactions are shown in Figure S9. The nearly identical regression
560 pattern for the $H_2O + O^1D$ and the total production rate with the MEI demonstrates that changes in
561 this reaction are driving changes in OH in the tropics during El Niño events.
562
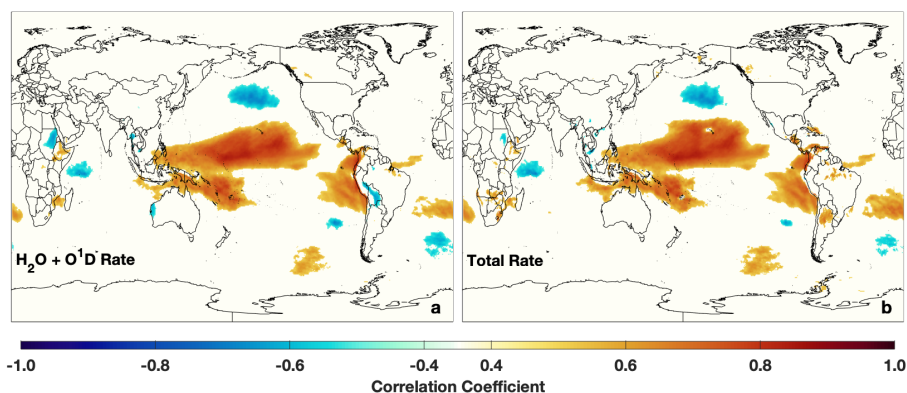
563
564 *Figure 11: Correlation of the production rate of OH from the $H_2O + O^1D$ reaction (a) for DJF and the total OH production rate as*
565 *defined in the text (b) with the MEI for the PBL level are shown.*

566   To understand the relationship between the OH production rate and ENSO in the PBL, we examine
567 the changes in $H_2O_{(v)}$ and O^1D (Fig. 12). The spatial correlation of $H_2O_{(v)}$ and the MEI in the PBL
568 exhibits a tripole pattern similar to that seen in the tropospheric column (Fig. 8a). While $H_2O_{(v)}$ is
569 correlated with the MEI in the equatorial Pacific, which would lead to increases in OH production,
570 $H_2O_{(v)}$ is anti-correlated with the MEI near the Hawaiian Islands and in the south Pacific, which
571 would lead to decreased OH production in these regions. Because OH increases in these areas
572 during El Niño events, the decreased $H_2O_{(v)}$ must be offset by increases in O^1D to result in a net
573 positive correlation of the total OH production rate.
574
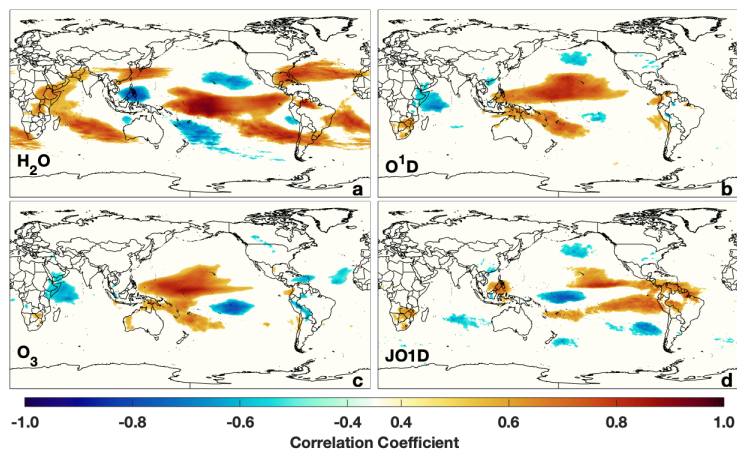
575
576 *Figure 12: Correlation of the indicated species with the MEI for the PBL level for DJF.*

577   Changes in O^1D and its photochemical drivers, O_3 and the rate of O_3 photolysis to O^1D (JO^{1}D), are
578 driving the ENSO-related changes in OH in the PBL. O^1D shows distinct regions of positive
579 correlation with ENSO extending from the Philippines to the eastern Pacific Ocean and another
580 region of positive correlation off the coast of Papua New Guinea (Fig. 12b). O^1D abundance is
581 controlled both by O_3 concentrations and incoming solar radiation at wavelengths less than 320
582 nm. Positive correlation between ENSO and O_3 in the PBL is limited to the western Pacific Ocean,
583 where horizontal advection of relatively high O_3 air from Indonesia to the Pacific Ocean is increased
584 during El Niño events due to changes in the Walker Circulation. Changes in O_3 and O^1D off the coast

585 of Papua New Guinea are potentially linked to the South Pacific Convergence Zone, which has a
586 strong dependence on ENSO (Borlace et al., 2014). JO^1D exhibits two regions of positive correlation
587 extending from South America, one that reaches Hawaii in the NH and another that spans almost to
588 the coast of Australia in the SH (Fig. 12d). These increases in O^1D are likely associated with changes
589 in stratospheric O_3, which can decrease by several Dobson Units in the tropics during El Niño events
590 (Randel et al., 2009).
591
592 5.3   The Upper Free Troposphere
593 5.3.1 The Relationship between UFT OH and ENSO
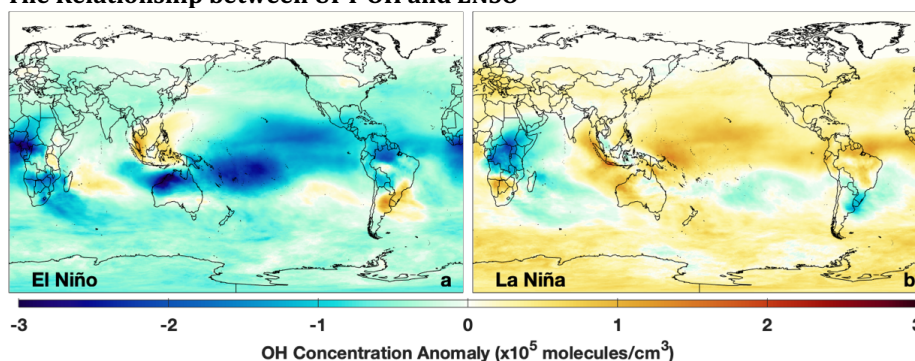
594
595 *Figure 13: Same as Figure 6 except for the UFT.*

596 Similar to the relationship between ENSO and TCOH, OH in the UFT shows a strong anticorrelation
597 with the MEI over much of the tropics (Fig. 10a) resulting in large-scale decreases during El Niño
598 events. Decreases are highest over Northern Australia and the west-central Pacific, on the order of
599 1-2×10^5 molecules/cm^3 or 15-20% lower than in neutral years. During La Niña events, OH
600 increases with respect to neutral years over much of the globe, although the magnitude of the
601 increases is lower than for El Niño events. As with TCOH, one notable exception is over central
602 Africa, where UFT OH decreases between 1-2×10^5 molecules/cm^3.
603
604 EOF analysis on UFT OH followed by correlation of the temporal component (*i.e.,* the principal
605 component) with the MEI demonstrates that ENSO is the dominant mode of OH variability in the
606 UFT throughout much of the year. The MEI correlates with UFT OH ($r^2 > 0.5$) for DJF, MAM, and
607 SON, and explains 36% of the variance or greater in each of the seasons (Table 1), demonstrating
608 that the relationship between ENSO and OH is even stronger in the UFT than in the tropospheric
609 column as a whole. As with the other atmospheric levels, there is little correlation between OH and
610 the MEI for JJA.
611
612 5.3.2 The Relationship between UFT OH drivers and ENSO
613 While changes in the $O^1D + H_2O$ reaction drive ENSO-related changes in OH production in the PBL,
614 the $NO + HO_2$ reaction drives OH production in the UFT. The nearly identical correlation patterns
615 between the $NO + HO_2$ reaction (Fig. 14) and the total OH production rate in the UFT layer suggest
616 that changes in NO and/or HO_2 during El Niño are driving interannual OH variability in the UFT,
617 leading to decreased OH production over most of the tropical Pacific. This dependence on the $NO + $
618 HO_2 reaction is consistent with its overall contribution to the total production rate as shown in
619 Figure 5. Similar plots for the other OH production reactions are shown in Figure S10.
620
621 Regression analysis suggests that changes in NO are driving the relationship between OH and ENSO
622 in the UFT in MERRA2 GMI. The MEI-NO correlation exhibits a strong dipole pattern in the tropics

623 (Fig. 15), with areas of positive correlation over southeast Asia and the maritime continent and a
624 large area of anti-correlation over much of the Pacific. HO_2 exhibits the opposite pattern, with
625 increased concentrations over much of the Pacific during El Niño. This is consistent with the NO
626 pattern, as decreased NO concentrations favor partitioning of HO_X (HO_X = OH + HO_2) towards HO_2.
627

Figure 14 content:

NO + HO$_2$ Rate (a) and **Total Rate** (b)

Correlation Coefficient scale: -1.0, -0.8, -0.6, -0.4, 0.4, 0.6, 0.8, 1.0
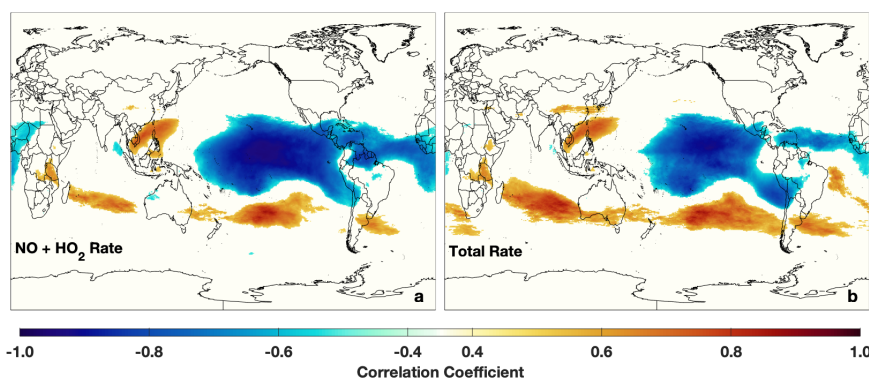
628
629 *Figure 14: Correlation of the production rate of OH from the NO + HO$_2$ reaction (a) for DJF and the total OH production rate as*
630 *defined in the text (b) with the MEI for the UFT level are shown.*

631 Similarities between NO and O_3 correlation with the MEI in the UFT suggest similar mechanisms in
632 controlling the spatial distribution of these species. The relationship between O_3 and the MEI
633 shown in Figure 15b is similar to that found in Oman et al. (2013) using satellite data. They
634 demonstrated that areas of increased O_3 over Indonesia coincided with increased downward flow
635 in the region associated with changes in the Walker circulation. Decreases in O_3 over the Pacific
636 coincided with increased upward motion, convectively lofting low O_3 air throughout the column.
637 Similarly, regions of anomalously low NO in the UFT during El Niño events are associated with
638 regions of anomalous upward motion (Fig. S7), suggesting that decreases in upper tropospheric NO
639 results from the convective lofting of NO_X-poor air from lower in the tropospheric column.
640
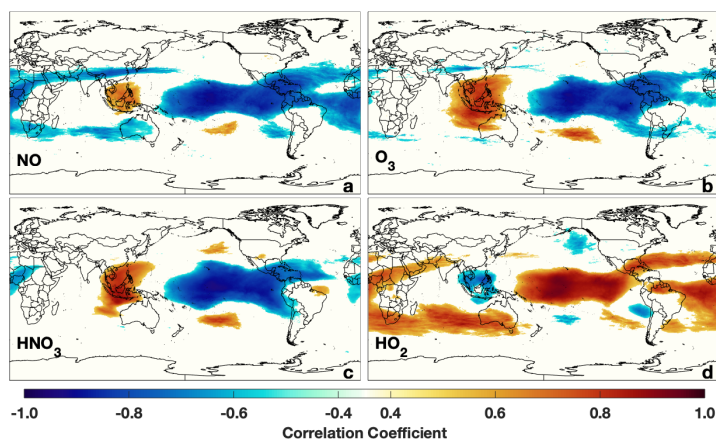
641
642 *Figure 15: Correlation of the indicated species with the MEI for the UFT level for DJF.*

643 The anti-correlation between ENSO and NO also suggests that lightning emissions of NO over the
644 tropical Pacific does not significantly increase OH production in the region. Lightning NO emissions
645 in MERRA2 GMI show a correlation pattern similar to that of $H_2O_{(v)}$ (Fig. 8c), with increased

646   lightning over the equatorial Pacific and decreased lightning poleward of this region during El Niño
647   events. The correlation pattern from MERRA2 GMI output agrees closely with flash rate data
648   observed from the Lightning Imaging Sensor (LIS). The only region of significant difference
649   between the satellite and MERRA2 GMI is in the equatorial Pacific, where the region of positive
650   correlation extends from Papua New Guinea to the South American coast in the simulation but only
651   about half that distance in the satellite product. These results are in contrast to the findings of
652   Turner et al. (2018), who found that lightning NO emissions were the primary driver in the
653   relationship between OH and ENSO. This difference could result from differences in the handling of
654   biomass burning emissions in the two models, as MERRA2 GMI emissions were based on
655   observations and varied seasonally. Our analysis also cannot disentangle the impact on ENSO-
656   related changes in lighting NO emissions over land on OH in the remote atmosphere.
657
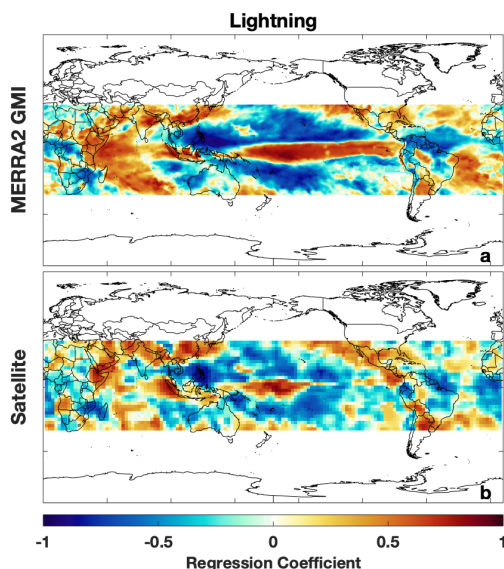
658
659   *Figure 16: The regression of lightning NO emissions at 300 hPa (a) and the lightning flash rate from the LIS/OTD time series (b)*
660   *against the MEI. Lightning data are restricted to within 35 degrees of the equator because of the spatial coverage of the*
661   *Tropical Rainfall Monitoring Mission (TRMM) satellite, on which LIS is located.*

662   This relationship with lightning, evident in both the satellite and model, is in contrast to the
663   relationship with all reactive nitrogen species (NO_y) in the UFT. NO and NO_2 in the UFT layer show
664   decreases over most of the Pacific during El Niño conditions.   This seeming discrepancy is due to
665   the small change in the magnitude of lightning NO emissions over the Pacific. Even though lightning
666   NO increases by 100% or more over the equatorial Pacific during El Niño events, the absolute
667   difference is orders of magnitude lower than that seen over land. This suggests that, while local
668   lightning emissions might be perturbing NO_X abundance, other mechanisms, such as convective
669   lofting and horizontal advection are driving the modeled relationship with ENSO. The similar
670   regression pattern of longer lived species, such as HNO_3 (Fig. 15c) and PAN (not shown), to NO in
671   the UFT supports this idea, showing that transport of reactive nitrogen from other regions,
672   including lightning from other areas, is likely reduced during El Niño events
673
674   **5.4   Variability in the MFT and LFT**
675   As in the UFT, ENSO is the dominant mode of variability in the MFT in DJF, with strong correlation
676   between the MEI and the temporal component of the first EOF (r^2 = 0.81) and the first EOF

677 explaining 20.8% of the total variance. Likewise, the largest OH anomalies in the LFT during both
678 El Niño and La Niña are centered over Australia and South Africa (Fig. 17), similar to patterns seen
679 in the UFT. Unlike in the UFT, however, there is a large region extending from the coast of South
680 America into the Pacific where OH concentration is positively correlated with ENSO. These changes
681 are driven by increase in $H_2O_{(v)}$, and subsequent increased OH production from the $H_2O + O^1D$
682 reaction.
683
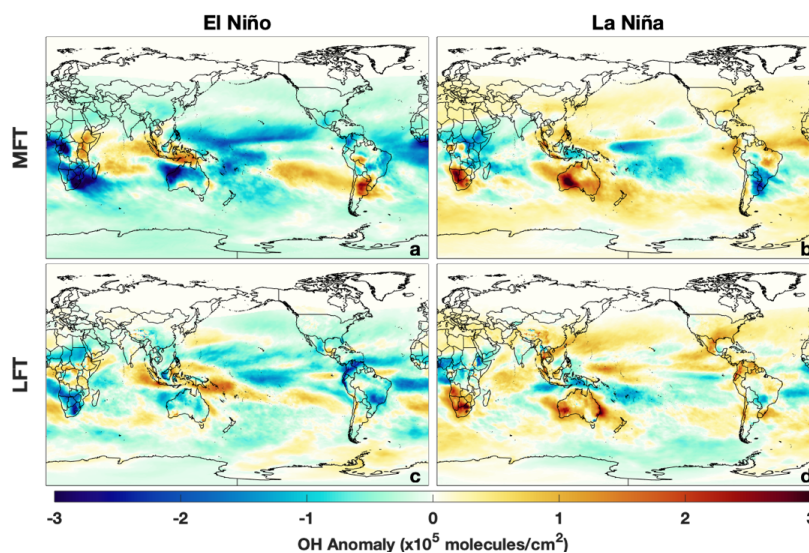
684
685 *Figure 17: Same as Figure 6 except for the MFT and LFT.*

686 ENSO-related changes in OH concentration in the LFT are smaller in magnitude than for the other
687 atmospheric levels (Fig. 17), with maximum increases in OH during El Niño on the order of 1 – 1.5 x
688 10^5 molecules/cm³. The spatial extent of significant correlation between the MEI and OH
689 concentration in the LFT is smaller than for the other atmospheric levels (Fig. 10), with the most
690 prominent feature being an area of positive correlation near Indonesia. Consistent with the more
691 limited impact, ENSO is correlated with the 2nd EOF of OH concentration for the LFT ($r^2 = 0.55$),
692 explaining only 11.7% of the total variability (Table 1).
693
694 It is likely that competing effects from the different drivers limit the interannual variability in OH in
695 the LFT and MFT, explaining the smaller regions of correlation with ENSO. For these levels, no
696 single OH production reaction clearly explains the relationship between ENSO and OH. In contrast
697 to the PBL and UFT, where the relationship between the total OH production rate closely mirrored
698 the production rates from the $O^1D + H_2O$ and $NO + HO_2$ reactions, respectively, there are no
699 analogous relationships for the LFT and MFT. At these levels, no reaction clearly dominates total
700 OH production (Fig. 5). Increases in H_2O in the mid troposphere, which would tend to increase OH,
701 are offset by decreases in NO and O_3. These competing effects likely explain why the absolute
702 changes in OH are comparatively smaller in the LFT than in the other layers.
703
704 **5.5   Comparing Simulated OH Relationships with ENSO in MERRA2 GMI with the CCMI**
705 **   models**
706 To understand whether the relationship between OH and ENSO found in MERRA2 GMI is robust, we
707 examine model simulations from the CCMI. To compare the relationship between OH and ENSO

708   among the different models, we performed the same regression analysis on TCOH for the CCMI
709   models as for MERRA2 GMI. Figure 18 shows the number of models that demonstrate a meaningful
710   correlation between TCOH and the MEI, defined as the absolute value of r greater than 0.5, for each
711   grid cell. To facilitate comparison, OH for each model has been regridded to the resolution of the
712   model with the lowest horizontal resolution (2.81° longitude x 2.77° latitude). This regridding does
713   not substantially alter the correlation patterns examined here.
714
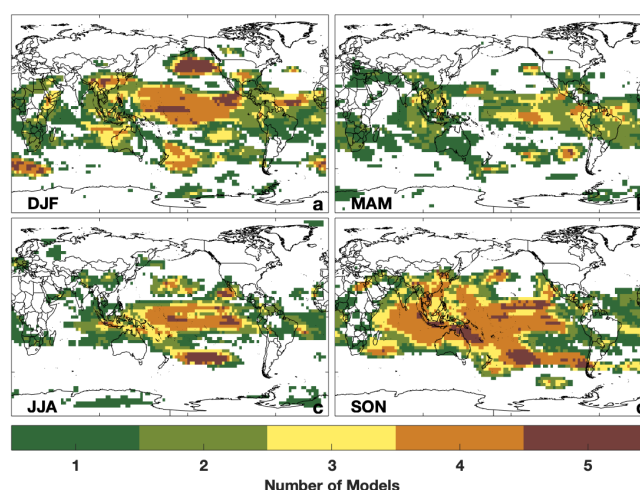
715
716   *Figure 18: The number of CCMI models and MERRA2 GMI that show a correlation between tropospheric column OH and ENSO*
717   *over the period 1980 to 2010. Only regressions with an absolute value of r greater than 0.5 are included. All models have been*
718   *regridded to a common horizontal grid. This regridding does not substantially alter the correlation patterns examined here.*

719   In agreement with MERRA2 GMI, TCOH varies with ENSO over a large fraction of the tropics in most
720   of the CCMI models, with broadly similar spatial regression patterns for most models across all
721   seasons except for MAM (Fig. 18). In DJF, most models show strong correlation between ENSO and
722   column OH over the central Pacific and south of the Aleutian Islands, with at least four models
723   showing correlation in each of these areas. This agreement highlights the relationship of OH with
724   ENSO as well as with the PNA and Australian monsoon, as discussed in Section 6.0. Similar
725   agreement among models was found for SON and JJA, although the spatial extent of the highly
726   correlated region is much smaller for JJA. In SON, the expansion of the area of significant
727   correlation over most of the Indian Ocean likely results from the strong relationship between the
728   IOD and ENSO during this season. There is less agreement in MAM, with only 1 or 2 models
729   showing strong correlation in most regions.
730
731   EOF analysis of the different CCMI models likewise suggests that, in DJF, ENSO is the dominant
732   mode of TCOH variability. The spatial pattern of the first EOF of TCOH in DJF for the five models is
733   shown in Figure S11, and the principal component time series, along with the time series of the
734   MEI, is shown in Figure S12. MERRA2 GMI, WACCM, and MRI show a strong correlation between
735   the MEI and the first EOF (r^2 > 0.64). For each of these models ENSO is the cause of 29 – 48% of the
736   total variance in TCOH. The correlation between the first EOF and the MEI for CHASER is weaker
737   (r^2 = 0.28), although the spatial component shows similarities to the other models. Correlation
738   between the MEI and the EOFs for the UFT and MFT levels increases to 0.56 and 0.45, respectively,
739   showing that ENSO is still important in controlling the interannual variability of CHASER, at least in
740   the UFT. Similarly, EMAC has no correlation between the 1st EOF of TCOH and the MEI, but does for

741 the UFT layer ($r^2 = 0.64$). This EOF explains 20% of the total variance for this level but has a
742 substantially different spatial pattern than for the other models.
743
744 The agreement among the majority of the models suggests that the relationship between ENSO and
745 TCOH is robust. While SSTs and emissions are identical among the models, meteorology, chemical
746 mechanisms, and parameterizations, such as that for lightning and convection, vary widely. Despite
747 the differences in these chemical and dynamical drivers of OH, the spatial patterns of the ENSO
748 TCOH relationship are similar for most models. While it is beyond the scope of this paper,
749 determining the cause of inter-model differences in this relationship between OH and climate
750 modes could further our understanding of the mechanisms driving interannual OH variability.
751
752 **6.0 Relationship between simulated OH and NH Climate Modes, Monsoons, and the IOD**
753 We now investigate the relationship between OH and the NH modes of variability, monsoons, and
754 the IOD. In Section 6.1, we evaluate the relationships in MERRA2 GMI, demonstrating that these
755 other climate features exert a much more spatially limited influence on OH as compared to ENSO
756 (Fig. 4). Despite the comparatively limited extent of influence, each of these modes of variability
757 can strongly influence the atmospheric oxidative capacity on the local scale. In Section 6.2, we
758 compare the results from MERRA2 GMI to CCMI simulations, demonstrating that the relationship
759 between OH and the IOD and NH modes is robust among models, while the relationship between
760 monsoons and OH is primarily limited to MERRA2 GMI.
761
762 **6.1 Simulated OH and the NH Climate Modes, Monsoons, and the IOD in MERRA2 GMI**
763 Northern Hemispheric modes of variability are strongly correlated ($r>0.5$) with the MEI over ~10%
764 of the globe during DJF but have a comparatively smaller effect on global OH than ENSO. During the
765 positive phases of the NAO and the PNA, defined as the respective index being greater than 0.4,
766 TCOH increases by up to 25% in the northern Atlantic and decreases by 10 – 20% in the northern
767 Pacific, respectively (Fig. S13). Because OH production is almost an order of magnitude lower in
768 the NH mid-latitudes than in the tropics (Fig. 5c), however, the resultant decrease in global mean
769 mass-weighted OH (e.g., Lawrence et al., 2001) during the positive phase of the NAO is only 0.77%,
770 as compared to decreases of 2.2% during an El Niño event. Similar results are found for the other
771 NH modes.
772
773 The effects of the monsoons on OH interannual variability are much more localized than for ENSO
774 and vary markedly among the different monsoons (Fig. 4). For example, Figure S14a shows the
775 partial correlation coefficient (e.g., Sekiya and Sudo, 2012) of TCOH with the Australian monsoon,
776 taking into account the correlation of the Australian monsoon index with the MEI, which has an r^2
777 of 0.65 for DJF. Correlation is almost exclusively restricted to areas near the Australian continent.
778 In this region, however, monsoons with an index in the 75th percentile or higher result in TCOH that
779 is 15-20% (up to 7×10^{11} molecules/cm^2) higher than for monsoons with an index between the 25th
780 and 75th percentile (Fig. S15). These increases in OH column for the strongest monsoons are larger
781 in magnitude than typical changes associated with ENSO, although they are limited to a smaller
782 region, suggesting that the Australian monsoon can significantly perturb the local atmospheric
783 oxidative capacity.
784
785 In contrast, despite its larger scale, the Asian monsoon only shows correlation with TCOH over a
786 small portion of the subcontinent (Fig. 4b&d). Interestingly, this correlation is only present during
787 MAM and SON, not during JJA when the Asian monsoon is at full strength. Lelieveld et al. (2018)
788 have shown using *in situ* observations that upper tropospheric OH is increased during the Asian
789 monsoon. The lack of correlation demonstrated here suggests either that there is not significant
790 interannual variability in this increase or that the model is not accurately capturing the chemical

791 variability within the monsoon anticyclone. The correlation with the monsoon index for MAM and
792 SON could result from interannual variability in the start and end of the monsoon. Since these
793 seasons are at the fringe of the monsoon, yearly variations in the start and end date would lead to
794 larger variability than that seen during JJA, when the monsoon is active every year.
795
796 The IOD also shows a strong relationship with OH, although due to its annual cycle, the relationship
797 is only present during SON (Fig. 4d). Taking into account the correlation between ENSO and the
798 IOD (r^2 = 0.30), the partial correlation between the Dipole Mode Index (DMI) and TCOH becomes
799 mostly restricted to the western Indian Ocean (Fig. S14b), where TCOH is anticorrelated with the
800 DMI, resulting in decreases in TCOH on the order of 10% (about 1.5×10^{11} molecules/cm^2).
801
802 **6.2 Simulated OH and the NH Climate Modes, Monsoons, and the IOD in the CCMI models**
803 The MERRA2 GMI and the CCMI simulations exhibit nearly identical spatial relationships between
804 TCOH and the NH climate modes and the IOD, demonstrating that these relationships are robust
805 among multiple models. For example, all 5 models show two broad regions of correlation between
806 the NAO and TCOH, corresponding to the dipole pattern of the NAO (Fig. 19a). Similar agreement is
807 found for the other NH modes (Fig. S16). Likewise, most models show the same pattern of
808 correlation between the IOD and TCOH (Fig. 19c), consistent with their agreement for ENSO since
809 the two modes are closely related.
810
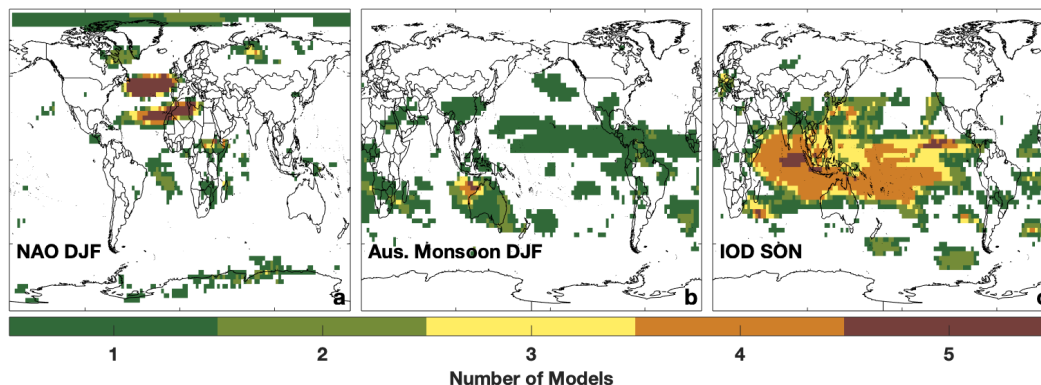
811
812 *Figure 19: Same as Figure 18 except for the NAO (a) and the Australian Monsoon (b) in DJF and for the IOD in SON (c).*

813 In contrast to the other modes of variability, the relationship between TCOH and the different
814 monsoons varies widely among the models. Agreement is highest for the Australian monsoon (Fig.
815 19b), where most models see correlation off the northwestern coast of the continent. For the other
816 monsoons considered here, there is no consistent relationship with OH, with most areas only
817 showing correlation with one model (Fig. S17). While models and observations have shown the
818 monsoons can change OH abundance, particularly in the UFT (Lelieveld et al., 2018), the lack of
819 correlation among the models suggests that those changes are not highly variable from year to year.
820
821 **7.0 Conclusions**
822 Because of limited *in situ* observations and inter-model differences, there is significant uncertainty
823 in the processes driving interannual OH variability, despite its importance in controlling the
824 removal of many atmospheric trace gases. Here, we have explored the relationship between OH
825 and multiple modes of climate variability, including ENSO, the IOD, NH modes of variability, and
826 monsoons in order to understand how these large-scale dynamical features influence OH through
827 control of its dynamical and photochemical drivers.

828
829 Using output from the MERRA2 GMI simulation, we have shown that during DJF, when considered
830 together, these climate features can explain OH variability over approximately 40% of the globe.
831 ENSO is the dominant mode of variability in all seasons except for JJA and can explain 20 – 30 % of
832 the variance in TCOH and results in an average decrease in global, mass weighted OH of 2.2%
833 during El Niño events. Effects from the other modes of variability considered here are more limited
834 in spatial scale but can strongly alter the atmospheric oxidative capacity on the local scale. For
835 example, changes in TCOH for the NAO, IOD, and Australian monsoon can reach 0.5, 1.5, and 7 x
836 10^{11} molecules/cm^2, respectively, compared to 2 x 10^{11} molecules/cm^2 for ENSO.
837
838 Changes in OH with ENSO are driven by different processes in the upper and lower troposphere. In
839 the PBL, where OH production is dominated by the reaction of O^{1}D with water, changes in the
840 distribution of these species leads to a positive correlation between OH and ENSO. Increases in
841 $H_2O_{(v)}$ during El Niño are associated with increased convection and warmer SSTs, while increases in
842 O^{1}D result from increased horizontal advection of O$_3$ in the western Pacific and increased
843 photolysis rates resulting from reduced stratospheric O$_3$ in the eastern Pacific. In the upper
844 troposphere, NO controls the OH abundance over the tropical Pacific. Despite increased lightning
845 NO$_X$ emissions in some areas of the Pacific, increased convective lofting of low NO air from near the
846 surface and advection of air with lower reactive nitrogen than during neutral years, leads to
847 reduced OH during El Niño events.
848
849 Absolute changes in OH concentration during El Niño and La Niña events in the LFT and, to a lesser
850 extent, the MFT were modest when compared to changes in OH in the PBL and UFT. At these levels,
851 OH production is driven by competing effects from the O^{1}D + H$_2$O and NO + HO$_2$ reactions. As a
852 result, ENSO only explains 11.7% of the variability in the LFT and is associated with the second
853 EOF. Because OH variability in the LFT drives variability in the oxidation of CH$_4$, further research is
854 warranted to understand the dominant mode of OH variability at this level, including any impacts in
855 emissions trends, which appear to be the dominant mode of variability in the PBL.
856
857 The relationship between the individual climate modes seen in MERRA2 GMI is also seen in the
858 majority of the CCMI models, suggesting that the relationship between the modes and OH is robust.
859 4 of the 5 models examined here show similar relationships between ENSO and TCOH for all
860 seasons except MAM, and three of those models suggest that ENSO is the dominant mode of OH
861 variability in DJF, responsible for between 30 and 50% of total variance. Similar agreement is
862 found for the NH modes of variability and the IOD, while there is little agreement among models
863 between the relationship of the individual monsoons and OH.
864
865 Despite the agreement among models in the importance of the driving factors of OH variability,
866 there is still a lack of observations to demonstrate that the models are accurate. We have shown
867 here that satellite observations of H$_2$O, CO, and lightning flashes are able to capture the respective
868 variability of each variable as well as the relationship with ENSO, in excellent agreement with the
869 model simulation. While further understanding of the relationship between these species and
870 ENSO is needed, the results presented here suggest that combining the observations of OH drivers
871 and the various climate modes could lead to additional methods to constrain OH from space.
872
873 **Data Availability**
874 All output from MERRA2 GMI is publicly available at https://acd-
875 ext.gsfc.nasa.gov/Projects/GEOSCCM/MERRA2GMI/. Output from the EMAC, MRI, and CHASER
876 models is available from the Centre for Environmental Data Analysis at
877 http://data.ceda.ac.uk/badc/wcrp-ccmi/data/CCMI-1/output. Output from WACCM are available

878 at http://www.earthsystemgrid.org. Satellite data are available at https://disc.gsfc.nasa.gov. Data
879 from the ATom campaign are located at https://espoarchive.nasa.gov/archive/browse/atom.
880
881 **Author Contributions**
882 DCA performed the analysis and wrote the manuscript. All authors contributed ideas for the
883 analysis and helped revise and improve the manuscript.
884
885 **Competing Interests**
886 The authors declare no competing interests.
887
888 **Acknowledgements**

889 The authors acknowledge funding from the NASA ACMAP program (16-ACMAP16-0027). We
890 acknowledge the modeling groups for making their simulations available for this analysis, the joint
891 WCRP SPARC/IGAC Chemistry-Climate Model Initiative (CCMI) for organizing and coordinating the
892 model data analysis activity, and the British Atmospheric Data Centre (BADC) for collecting and
893 archiving the CCMI model output.

894
895

896
897 **References**
898
899 Allen, D., Pickering, K., Duncan, B., and Damon, M.: Impact of lightning NO emissions on North
900 American photochemistry as determined using the Global Modeling Initiative (GMI) model, Journal
901 of Geophysical Research, 115, 10.1029/2010jd014062, 2010.

902 Anderson, D. C., Nicely, J. M., Wolfe, G. M., Hanisco, T. F., Salawitch, R. J., Canty, T. P., Dickerson, R. R.,
903 Apel, E. C., Baidar, S., Bannan, T. J., Blake, N. J., Chen, D. X., Dix, B., Fernandez, R. P., Hall, S. R.,
904 Hornbrook, R. S., Huey, L. G., Josse, B., Jockel, P., Kinnison, D. E., Koenig, T. K., Le Breton, M., Marecal,
905 V., Morgenstern, O., Oman, L. D., Pan, L. L., Percival, C., Plummer, D., Revell, L. E., Rozanov, E., Saiz-
906 Lopez, A., Stenke, A., Sudo, K., Tilmes, S., Ullmann, K., Volkamer, R., Weinheimer, A. J., and Zeng, G.:
907 Formaldehyde in the Tropical Western Pacific: Chemical Sources and Sinks, Convective Transport,
908 and Representation in CAM-Chem and the CCMI Models, Journal of Geophysical Research-
909 Atmospheres, 122, 11201-11226, 10.1002/2016jd026121, 2017.

910 Barnston, A. G., and Livezey, R. E.: Classification, Seasonality and Persistence of Low-Frequency
911 Atmospheric Circulation Patterns, Monthly Weather Review, 115, 1083-1126, 10.1175/1520-
912 0493(1987)115<1083:CSAPOL>2.0.CO;2, 1987.

913 Borlace, S., Santoso, A., Cai, W., and Collins, M.: Extreme swings of the South Pacific Convergence
914 Zone and the different types of El Niño events, Geophysical Research Letters, 41, 4695-4703,
915 10.1002/2014gl060551, 2014.

916 Brune, W. H., Miller, D. O., Thames, A. B., Allen, H. M., Apel, E. C., Blake, D. R., Bui, T. P., Commane, R.,
917 Crounse, J. D., Daube, B. C., Diskin, G. S., DiGangi, J. P., Elkins, J. W., Hall, S. R., Hanisco, T. F., Hannun,
918 R. A., Hintsa, E. J., Hornbrook, R. S., Kim, M. J., McKain, K., Moore, F. L., Neuman, J. A., Nicely, J. M.,
919 Peischl, J., Ryerson, T. B., St. Clair, J. M., Sweeney, C., Teng, A. P., Thompson, C., Ullmann, K., Veres, P.
920 R., Wennberg, P. O., and Wolfe, G. M.: Exploring Oxidation in the Remote Free Troposphere: Insights
921 From Atmospheric Tomography (ATom), Journal of Geophysical Research: Atmospheres, 125,
922 10.1029/2019jd031685, 2020.

923 Cecil, D. J., Buechler, D. E., and Blakeslee, R. J.: Gridded lightning climatology from TRMM-LIS and
924 OTD: Dataset description, Atmospheric Research, 135, 404-414, 10.1016/j.atmosres.2012.06.028,
925 2014.

926 Creilson, J. K., Fishman, J., and Wozniak, A. E.: Intercontinental transport of tropospheric ozone: a
927 study of its seasonal variability across the North Atlantic utilizing tropospheric ozone residuals and
928 its relationship to the North Atlantic Oscillation, Atmos. Chem. Phys., 3, 2053-2066, 10.5194/acp-3-
929 2053-2003, 2003.

930 Deeter, M. N., Edwards, D. P., Francis, G. L., Gille, J. C., Mao, D., Martínez-Alonso, S., Worden, H. M.,
931 Ziskin, D., and Andreae, M. O.: Radiance-based retrieval bias mitigation for the MOPITT instrument:
932 the version 8 product, Atmospheric Measurement Techniques, 12, 4561-4580, 10.5194/amt-12-
933 4561-2019, 2019.

934 Dhomse, S. S., Kinnison, D., Chipperfield, M. P., Salawitch, R. J., Cionni, I., Hegglin, M. I., Abraham, N.
935 L., Akiyoshi, H., Archibald, A. T., Bednarz, E. M., Bekki, S., Braesicke, P., Butchart, N., Dameris, M.,
936 Deushi, M., Frith, S., Hardiman, S. C., Hassler, B., Horowitz, L. W., Hu, R.-M., Jöckel, P., Josse, B., Kirner,
937 O., Kremser, S., Langematz, U., Lewis, J., Marchand, M., Lin, M., Mancini, E., Marécal, V., Michou, M.,

938 Morgenstern, O., amp, apos, Connor, F. M., Oman, L., Pitari, G., Plummer, D. A., Pyle, J. A., Revell, L. E.,
939 Rozanov, E., Schofield, R., Stenke, A., Stone, K., Sudo, K., Tilmes, S., Visioni, D., Yamashita, Y., and
940 Zeng, G.: Estimates of ozone return dates from Chemistry-Climate Model Initiative simulations,
941 Atmospheric Chemistry and Physics, 18, 8409-8438, 10.5194/acp-18-8409-2018, 2018.

942 Duncan, B. N.: Interannual and seasonal variability of biomass burning emissions constrained by
943 satellite observations, Journal of Geophysical Research, 108, 10.1029/2002jd002378, 2003a.

944 Duncan, B. N.: Indonesian wildfires of 1997: Impact on tropospheric chemistry, Journal of
945 Geophysical Research, 108, 10.1029/2002jd003195, 2003b.

946 Duncan, B. N.: A modeling study of the export pathways of pollution from Europe: Seasonal and
947 interannual variations (1987–1997), Journal of Geophysical Research, 109,
948 10.1029/2003jd004079, 2004.

949 Duncan, B. N., Logan, J. A., Bey, I., Megretskaia, I. A., Yantosca, R. M., Novelli, P. C., Jones, N. B., and
950 Rinsland, C. P.: Global budget of CO, 1988–1997: Source estimates and validation with a global
951 model, Journal of Geophysical Research, 112, 10.1029/2007jd008459, 2007.

952 Gelaro, R., McCarty, W., Suarez, M. J., Todling, R., Molod, A., Takacs, L., Randles, C., Darmenov, A.,
953 Bosilovich, M. G., Reichle, R., Wargan, K., Coy, L., Cullather, R., Draper, C., Akella, S., Buchard, V.,
954 Conaty, A., da Silva, A., Gu, W., Kim, G. K., Koster, R., Lucchesi, R., Merkova, D., Nielsen, J. E., Partyka,
955 G., Pawson, S., Putman, W., Rienecker, M., Schubert, S. D., Sienkiewicz, M., and Zhao, B.: The Modern-
956 Era Retrospective Analysis for Research and Applications, Version 2 (MERRA-2), J Clim, Volume 30,
957 5419-5454, 10.1175/JCLI-D-16-0758.1, 2017.

958 Giglio, L., Randerson, J. T., and van der Werf, G. R.: Analysis of daily, monthly, and annual burned
959 area using the fourth-generation global fire emissions database (GFED4), Journal of Geophysical
960 Research: Biogeosciences, 118, 317-328, 10.1002/jgrg.20042, 2013.

961 Granier, C., Bessagnet, B., Bond, T., D'Angiola, A., Denier van der Gon, H., Frost, G. J., Heil, A., Kaiser, J.
962 W., Kinne, S., Klimont, Z., Kloster, S., Lamarque, J.-F., Liousse, C., Masui, T., Meleux, F., Mieville, A.,
963 Ohara, T., Raut, J.-C., Riahi, K., Schultz, M. G., Smith, S. J., Thompson, A., van Aardenne, J., van der
964 Werf, G. R., and van Vuuren, D. P.: Evolution of anthropogenic and biomass burning emissions of air
965 pollutants at global and regional scales during the 1980–2010 period, Climatic Change, 109, 163-
966 190, 10.1007/s10584-011-0154-1, 2011.

967 Guenther, A., Baugh, B., Brasseur, G., Greenberg, J., Harley, P., Klinger, L., Serça, D., and Vierling, L.:
968 Isoprene emission estimates and uncertainties for the central African EXPRESSO study domain,
969 Journal of Geophysical Research: Atmospheres, 104, 30625-30639, 10.1029/1999JD900391, 1999.

970 Guenther, A., Geron, C., Pierce, T., Lamb, B., Harley, P., and Fall, R.: Natural emissions of non-
971 methane volatile organic compounds, carbon monoxide, and oxides of nitrogen from North
972 America, Atmospheric Environment, 34, 2205-2230, https://doi.org/10.1016/S1352-
973 2310(99)00465-3, 2000.

974 Jöckel, P., Tost, H., Pozzer, A., Kunze, M., Kirner, O., Brenninkmeijer, C. A. M., Brinkop, S., Cai, D. S.,
975 Dyroff, C., Eckstein, J., Frank, F., Garny, H., Gottschaldt, K. D., Graf, P., Grewe, V., Kerkweg, A., Kern, B.,
976 Matthes, S., Mertens, M., Meul, S., Neumaier, M., Nützel, M., Oberländer-Hayn, S., Ruhnke, R., Runde,
977 T., Sander, R., Scharffe, D., and Zahn, A.: Earth System Chemistry integrated Modelling (ESCiMo)

978   with the Modular Earth Submodel System (MESSy) version 2.51, Geosci. Model Dev., 9, 1153-1200,
979   10.5194/gmd-9-1153-2016, 2016.

980   Krotkov, N. A., Lamsal, L. N., Celarier, E. A., Swartz, W. H., Marchenko, S. V., Bucsela, E. J., Chan, K. L.,
981   Wenig, M., and Zara, M.: The version 3 OMI NO2 standard product, Atmospheric Measurement
982   Techniques, 10, 3133-3149, 10.5194/amt-10-3133-2017, 2017.

983   Lawrence, M. G., Jöckel, P., and von Kuhlmann, R.: What does the global mean OH concentration tell
984   us?, Atmos. Chem. Phys., 1, 37-49, 10.5194/acp-1-37-2001, 2001.

985   Lelieveld, J., Bourtsoukidis, E., Bruhl, C., Fischer, H., Fuchs, H., Harder, H., Hofzumahaus, A., Holland,
986   F., Marno, D., Neumaier, M., Pozzer, A., Schlager, H., Williams, J., Zahn, A., and Ziereis, H.: The South
987   Asian monsoon-pollution pump and purifier, Science, 361, 270-273, 10.1126/science.aar2501,
988   2018.

989   Li, Q., Jacob, D. J., Bey, I., Palmer, P. I., Duncan, B. N., Field, B. D., Martin, R. V., Fiore, A. M., Yantosca, R.
990   M., Parrish, D. D., Simmonds, P. G., and Oltmans, S. J.: Transatlantic transport of pollution and its
991   effects on surface ozone in Europe and North America, Journal of Geophysical Research:
992   Atmospheres, 107, ACH 4-1-ACH 4-21, 10.1029/2001JD001422, 2002.

993   Mao, J., Ren, X., Brune, W. H., Olson, J. R., Crawford, J. H., Fried, A., Huey, L. G., Cohen, R. C., Heikes, B.,
994   Singh, H. B., Blake, D. R., Sachse, G. W., Diskin, G. S., Hall, S. R., and Shetter, R. E.: Airborne
995   measurement of OH reactivity during INTEX-B, Atmos. Chem. Phys., 9, 163-173, 10.5194/acp-9-
996   163-2009, 2009.

997   Morgenstern, O., Hegglin, M. I., Rozanov, E., amp, apos, Connor, F. M., Abraham, N. L., Akiyoshi, H.,
998   Archibald, A. T., Bekki, S., Butchart, N., Chipperfield, M. P., Deushi, M., Dhomse, S. S., Garcia, R. R.,
999   Hardiman, S. C., Horowitz, L. W., Jöckel, P., Josse, B., Kinnison, D., Lin, M., Mancini, E., Manyin, M. E.,
1000   Marchand, M., Marécal, V., Michou, M., Oman, L. D., Pitari, G., Plummer, D. A., Revell, L. E., Saint-
1001   Martin, D., Schofield, R., Stenke, A., Stone, K., Sudo, K., Tanaka, T. Y., Tilmes, S., Yamashita, Y.,
1002   Yoshida, K., and Zeng, G.: Review of the global models used within phase 1 of the Chemistry–Climate
1003   Model Initiative (CCMI), Geoscientific Model Development, 10, 639-671, 10.5194/gmd-10-639-
1004   2017, 2017.

1005   Murray, L. T., Logan, J. A., and Jacob, D. J.: Interannual variability in tropical tropospheric ozone and
1006   OH: The role of lightning, Journal of Geophysical Research: Atmospheres, 118, 11,468-411,480,
1007   10.1002/jgrd.50857, 2013.

1008   Murray, L. T., Mickley, L. J., Kaplan, J. O., Sofen, E. D., Pfeiffer, M., and Alexander, B.: Factors
1009   controlling variability in the oxidative capacity of the troposphere since the Last Glacial Maximum,
1010   Atmospheric Chemistry and Physics, 14, 3589-3622, 10.5194/acp-14-3589-2014, 2014.

1011   Myers, D. S., and Waliser, D. E.: Three-Dimensional Water Vapor and Cloud Variations Associated
1012   with the Madden–Julian Oscillation during Northern Hemisphere Winter, Journal of Climate, 16,
1013   929-950, 10.1175/1520-0442(2003)016<0929:TDWVAC>2.0.CO;2, 2003.

1014   Naik, V., Voulgarakis, A., Fiore, A. M., Horowitz, L. W., Lamarque, J. F., Lin, M., Prather, M. J., Young, P.
1015   J., Bergmann, D., Cameron-Smith, P. J., Cionni, I., Collins, W. J., Dalsøren, S. B., Doherty, R., Eyring, V.,
1016   Faluvegi, G., Folberth, G. A., Josse, B., Lee, Y. H., MacKenzie, I. A., Nagashima, T., van Noije, T. P. C.,
1017   Plummer, D. A., Righi, M., Rumbold, S. T., Skeie, R., Shindell, D. T., Stevenson, D. S., Strode, S., Sudo, K.,

1018   Szopa, S., and Zeng, G.: Preindustrial to present-day changes in tropospheric hydroxyl radical and
1019   methane lifetime from the Atmospheric Chemistry and Climate Model Intercomparison Project
1020   (ACCMIP), Atmospheric Chemistry and Physics, 13, 5277-5298, 10.5194/acp-13-5277-2013, 2013.

1021   Nicely, J. M., Salawitch, R. J., Canty, T., Anderson, D. C., Arnold, S. R., Chipperfield, M. P., Emmons, L.
1022   K., Flemming, J., Huijnen, V., Kinnison, D. E., Lamarque, J.-F., Mao, J., Monks, S. A., Steenrod, S. D.,
1023   Tilmes, S., and Turquety, S.: Quantifying the causes of differences in tropospheric OH within global
1024   models, Journal of Geophysical Research: Atmospheres, n/a-n/a, 10.1002/2016JD026239, 2017.

1025   Nicely, J. M., Duncan, B. N., Hanisco, T. F., Wolfe, G. M., Salawitch, R. J., Deushi, M., Haslerud, A. S.,
1026   Jöckel, P., Josse, B., Kinnison, D. E., Klekociuk, A., Manyin, M. E., Marécal, V., Morgenstern, O., Murray,
1027   L. T., Myhre, G., Oman, L. D., Pitari, G., Pozzer, A., Quaglia, I., Revell, L. E., Rozanov, E., Stenke, A.,
1028   Stone, K., Strahan, S., Tilmes, S., Tost, H., Westervelt, D. M., and Zeng, G.: A machine learning
1029   examination of hydroxyl radical differences among model simulations for CCMI-1, Atmospheric
1030   Chemistry and Physics, 20, 1341-1361, 10.5194/acp-20-1341-2020, 2020.

1031   Oman, L. D., Ziemke, J. R., Douglass, A. R., Waugh, D. W., Lang, C., Rodriguez, J. M., and Nielsen, J. E.:
1032   The response of tropical tropospheric ozone to ENSO, Geophysical Research Letters, 38, n/a-n/a,
1033   10.1029/2011gl047865, 2011.

1034   Oman, L. D., Douglass, A. R., Ziemke, J. R., Rodriguez, J. M., Waugh, D. W., and Nielsen, J. E.: The ozone
1035   response to ENSO in Aura satellite measurements and a chemistry-climate simulation, Journal of
1036   Geophysical Research-Atmospheres, 118, 965-976, 10.1029/2012jd018546, 2013.

1037   Orbe, C., Oman, L. D., Strahan, S. E., Waugh, D. W., Pawson, S., Takacs, L. L., and Molod, A. M.: Large-
1038   Scale Atmospheric Transport in GEOS Replay Simulations, Journal of Advances in Modeling Earth
1039   Systems, 9, 2545-2560, 10.1002/2017ms001053, 2017.

1040   Orbe, C., Plummer, D. A., Waugh, D. W., Yang, H., Jöckel, P., Kinnison, D. E., Josse, B., Marecal, V.,
1041   Deushi, M., Abraham, N. L., Archibald, A. T., Chipperfield, M. P., Dhomse, S., Feng, W., and Bekki, S.:
1042   Description and Evaluation of the specified-dynamics experiment in the Chemistry-Climate Model
1043   Initiative, Atmospheric Chemistry and Physics, 20, 3809-3840, 10.5194/acp-20-3809-2020, 2020.

1044   Pan, L. L., Randel, W. J., Gary, B. L., Mahoney, M. J., and Hintsa, E. J.: Definitions and sharpness of the
1045   extratropical tropopause: A trace gas perspective, Journal of Geophysical Research: Atmospheres,
1046   109, n/a-n/a, 10.1029/2004JD004982, 2004.

1047   Prather, M. J., and Holmes, C. D.: Overexplaining or underexplaining methane's role in climate
1048   change, Proc Natl Acad Sci U S A, 114, 5324-5326, 10.1073/pnas.1704884114, 2017.

1049   Prinn, R. G., Huang, J., Weiss, R. F., Cunnold, D. M., Fraser, P. J., Simmonds, P. G., McCulloch, A., Harth,
1050   C., Salameh, P., O'Do, Wang, R. H. J., Porter, L., and Miller, B. R.: Evidence for Substantial Variations of
1051   Atmospheric Hydroxyl Radicals in the Past Two Decades, Science, 292, 1882-1888,
1052   10.1126/science.1058673, 2001.

1053   Randel, W. J., Garcia, R. R., Calvo, N., and Marsh, D.: ENSO influence on zonal mean temperature and
1054   ozone in the tropical lower stratosphere, Geophysical Research Letters, 36,
1055   10.1029/2009GL039343, 2009.

1056   Revell, L. E., Stenke, A., Tummon, F., Feinberg, A., Rozanov, E., Peter, T., Abraham, N. L., Akiyoshi, H.,
1057   Archibald, A. T., Butchart, N., Deushi, M., Jöckel, P., Kinnison, D., Michou, M., Morgenstern, O., amp,

apos, Connor, F. M., Oman, L. D., Pitari, G., Plummer, D. A., Schofield, R., Stone, K., Tilmes, S., Visioni, D., Yamashita, Y., and Zeng, G.: Tropospheric ozone in CCMI models and Gaussian process emulation to understand biases in the SOCOLv3 chemistry–climate model, Atmospheric Chemistry and Physics, 18, 16155-16172, 10.5194/acp-18-16155-2018, 2018.

Rigby, M., Montzka, S. A., Prinn, R. G., White, J. W. C., Young, D., O'Doherty, S., Lunt, M. F., Ganesan, A. L., Manning, A. J., Simmonds, P. G., Salameh, P. K., Harth, C. M., Muhle, J., Weiss, R. F., Fraser, P. J., Steele, L. P., Krummel, P. B., McCulloch, A., and Park, S.: Role of atmospheric oxidation in recent methane growth, Proc Natl Acad Sci U S A, 114, 5373-5377, 10.1073/pnas.1616426114, 2017.

Rowlinson, M. J., Rap, A., Arnold, S. R., Pope, R. J., Chipperfield, M. P., McNorton, J., Forster, P., Gordon, H., Pringle, K. J., Feng, W., Kerridge, B. J., Latter, B. L., and Siddans, R.: Impact of El Niño–Southern Oscillation on the interannual variability of methane and tropospheric ozone, Atmospheric Chemistry and Physics, 19, 8669-8686, 10.5194/acp-19-8669-2019, 2019.

Santoni, G. W., Daube, B. C., Kort, E. A., Jiménez, R., Park, S., Pittman, J. V., Gottlieb, E., Xiang, B., Zahniser, M. S., Nelson, D. D., McManus, J. B., Peischl, J., Ryerson, T. B., Holloway, J. S., Andrews, A. E., Sweeney, C., Hall, B., Hintsa, E. J., Moore, F. L., Elkins, J. W., Hurst, D. F., Stephens, B. B., Bent, J., and Wofsy, S. C.: Evaluation of the airborne quantum cascade laser spectrometer (QCLS) measurements of the carbon and greenhouse gas suite – CO2, CH4, N2O, and CO – during the CalNex and HIPPO campaigns, Atmospheric Measurement Techniques, 7, 1509-1526, 10.5194/amt-7-1509-2014, 2014.

Seibert, P., Beyrich, F., Gryning, S.-E., Joffre, S., Rasmussen, A., and Tercier, P.: Review and intercomparison of operational methods for determination of the mixing height, Atmospheric Environment, 34, 1001-1027, 2000.

Sekiya, T., and Sudo, K.: Role of meteorological variability in global tropospheric ozone during 1970-2008, Journal of Geophysical Research: Atmospheres, 117, n/a-n/a, 10.1029/2012jd018054, 2012.

Shi, L., Schreck, C., and Schröder, M.: Assessing the Pattern Differences between Satellite-Observed Upper Tropospheric Humidity and Total Column Water Vapor during Major El Niño Events, Remote Sensing, 10, 10.3390/rs10081188, 2018.

Solomon, S., Kinnison, D., Bandoro, J., and Garcia, R.: Simulation of polar ozone depletion: An update, Journal of Geophysical Research: Atmospheres, 120, 7958-7974, 10.1002/2015jd023365, 2015.

Spivakovsky, C. M., Logan, J. A., Montzka, S. A., Balkanski, Y. J., Foreman-Fowler, M., Jones, D. B. A., Horowitz, L. W., Fusco, A. C., Brenninkmeijer, C. A. M., Prather, M. J., Wofsy, S. C., and McElroy, M. B.: Three-dimensional climatological distribution of tropospheric OH: Update and evaluation, Journal of Geophysical Research: Atmospheres, 105, 8931-8980, 10.1029/1999jd901006, 2000.

Stein, O., Schultz, M. G., Bouarar, I., Clark, H., Huijnen, V., Gaudel, A., George, M., and Clerbaux, C.: On the wintertime low bias of Northern Hemisphere carbon monoxide found in global model simulations, Atmospheric Chemistry and Physics, 14, 9295-9316, 10.5194/acp-14-9295-2014, 2014.

Stone, D., Whalley, L. K., and Heard, D. E.: Tropospheric OH and HO2 radicals: field measurements and model comparisons, Chem Soc Rev, 41, 6348-6404, 10.1039/c2cs35140d, 2012.

1098   Strode, S. A., Ziemke, J. R., Oman, L. D., Lamsal, L. N., Olsen, M. A., and Liu, J.: Global changes in the
1099   diurnal cycle of surface ozone, Atmospheric Environment, 199, 323-333,
1100   10.1016/j.atmosenv.2018.11.028, 2019.

1101   Susskind, J., Blaisdell, J. M., and Iredell, L.: Improved methodology for surface and atmospheric
1102   soundings, error estimates, and quality control procedures: the atmospheric infrared sounder
1103   science team version-6 retrieval algorithm, Journal of Applied Remote Sensing, 8,
1104   10.1117/1.Jrs.8.084994, 2014.

1105   Tian, B., Yung, Y. L., Waliser, D. E., Tyranowski, T., Kuai, L., Fetzer, E. J., and Irion, F. W.: Intraseasonal
1106   variations of the tropical total ozone and their connection to the Madden-Julian Oscillation,
1107   Geophysical Research Letters, 34, 10.1029/2007gl029451, 2007.

1108   Turner, A. J., Frankenberg, C., Wennberg, P. O., and Jacob, D. J.: Ambiguity in the causes for decadal
1109   trends in atmospheric methane and hydroxyl, Proceedings of the National Academy of Sciences,
1110   114, 5367, 10.1073/pnas.1616020114, 2017.

1111   Turner, A. J., Fung, I., Naik, V., Horowitz, L. W., and Cohen, R. C.: Modulation of hydroxyl variability
1112   by ENSO in the absence of external forcing, Proc Natl Acad Sci U S A, 115, 8931-8936,
1113   10.1073/pnas.1807532115, 2018.

1114   Voulgarakis, A., Naik, V., Lamarque, J. F., Shindell, D. T., Young, P. J., Prather, M. J., Wild, O., Field, R.
1115   D., Bergmann, D., Cameron-Smith, P., Cionni, I., Collins, W. J., Dalsøren, S. B., Doherty, R. M., Eyring,
1116   V., Faluvegi, G., Folberth, G. A., Horowitz, L. W., Josse, B., MacKenzie, I. A., Nagashima, T., Plummer, D.
1117   A., Righi, M., Rumbold, S. T., Stevenson, D. S., Strode, S. A., Sudo, K., Szopa, S., and Zeng, G.: Analysis of
1118   present day and future OH and methane lifetime in the ACCMIP simulations, Atmospheric
1119   Chemistry and Physics, 13, 2563-2587, 10.5194/acp-13-2563-2013, 2013.

1120   Wang, P., Schade, G., Estes, M., and Ying, Q.: Improved MEGAN predictions of biogenic isoprene in
1121   the contiguous United States, Atmospheric Environment, 148, 337-351,
1122   10.1016/j.atmosenv.2016.11.006, 2017.

1123   Watanabe, S., Hajima, T., Sudo, K., Nagashima, T., Takemura, T., Okajima, H., Nozawa, T., Kawase, H.,
1124   Abe, M., Yokohata, T., Ise, T., Sato, H., Kato, E., Takata, K., Emori, S., and Kawamiya, M.: MIROC-ESM
1125   2010: model description and basic results of CMIP5-20c3m experiments, Geosci. Model Dev., 4, 845-
1126   872, 10.5194/gmd-4-845-2011, 2011.

1127   Wild, O., Voulgarakis, A., amp, apos, Connor, F., Lamarque, J.-F., Ryan, E. M., and Lee, L.: Global
1128   sensitivity analysis of chemistry–climate model budgets of tropospheric ozone and OH:
1129   exploring model diversity, Atmospheric Chemistry and Physics, 20, 4047-4058, 10.5194/acp-20-
1130   4047-2020, 2020.

1131   Wolfe, G. M., Nicely, J. M., St Clair, J. M., Hanisco, T. F., Liao, J., Oman, L. D., Brune, W. B., Miller, D.,
1132   Thames, A., Gonzalez Abad, G., Ryerson, T. B., Thompson, C. R., Peischl, J., McCain, K., Sweeney, C.,
1133   Wennberg, P. O., Kim, M., Crounse, J. D., Hall, S. R., Ullmann, K., Diskin, G., Bui, P., Chang, C., and Dean-
1134   Day, J.: Mapping hydroxyl variability throughout the global remote troposphere via synthesis of
1135   airborne and satellite formaldehyde observations, Proc Natl Acad Sci U S A, 116, 11171-11180,
1136   10.1073/pnas.1821661116, 2019.

1137   Wolter, K., and Timlin, M. S.: El Niño/Southern Oscillation behaviour since 1871 as diagnosed in an
1138   extended multivariate ENSO index (MEI.ext), International Journal of Climatology, 31, 1074-1087,
1139   10.1002/joc.2336, 2011.

1140   Wong, S., and Dessler, A. E.: Regulation of H2O and CO in tropical tropopause layer by the Madden-
1141   Julian oscillation, Journal of Geophysical Research: Atmospheres, 112, 10.1029/2006JD007940,
1142   2007.

1143   Yim, S.-Y., Wang, B., Liu, J., and Wu, Z.: A comparison of regional monsoon variability using monsoon
1144   indices, Climate Dynamics, 43, 1423-1437, 10.1007/s00382-013-1956-9, 2013.

1145   Yukimoto, S., Adachi, Y., Hosaka, M., Sakami, T., Yoshimura, H., Hirabara, M., Tanaka, T. Y., Shindo, E.,
1146   Tsujino, H., Deushi, M., Mizuta, R., Yabu, S., Obata, A., Nakano, H., Koshiro, T., Ose, T., and Kitoh, A.: A
1147   New Global Climate Model of the Meteorological Research Institute: MRI-CGCM3 —Model
1148   Description and Basic Performance&mdash, Journal of the Meteorological Society of Japan. Ser. II,
1149   90A, 23-64, 10.2151/jmsj.2012-A02, 2012.

1150   Zhang, Z., Zimmermann, N. E., Calle, L., Hurtt, G., Chatterjee, A., and Poulter, B.: Enhanced response
1151   of global wetland methane emissions to the 2015–2016 El Niño-Southern Oscillation event,
1152   Environmental Research Letters, 13, 10.1088/1748-9326/aac939, 2018.

1153   Zhao, Y., Saunois, M., Bousquet, P., Lin, X., Berchet, A., Hegglin, M. I., Canadell, J. G., Jackson, R. B.,
1154   Hauglustaine, D. A., Szopa, S., Stavert, A. R., Abraham, N. L., Archibald, A. T., Bekki, S., Deushi, M.,
1155   Jöckel, P., Josse, B., Kinnison, D., Kirner, O., Marécal, V., amp, apos, Connor, F. M., Plummer, D. A.,
1156   Revell, L. E., Rozanov, E., Stenke, A., Strode, S., Tilmes, S., Dlugokencky, E. J., and Zheng, B.: Inter-
1157   model comparison of global hydroxyl radical (OH) distributions and their impact on atmospheric
1158   methane over the 2000–2016 period, Atmospheric Chemistry and Physics, 19, 13701-
1159   13723, 10.5194/acp-19-13701-2019, 2019.

1160   Ziemke, J. R., Douglass, A. R., Oman, L. D., Strahan, S. E., and Duncan, B. N.: Tropospheric ozone
1161   variability in the tropics from ENSO to MJO and shorter timescales, Atmospheric Chemistry and
1162   Physics, 15, 8037-8049, 10.5194/acp-15-8037-2015, 2015.

1163   Ziemke, J. R., Oman, L. D., Strode, S. A., Douglass, A. R., Olsen, M. A., McPeters, R. D., Bhartia, P. K.,
1164   Froidevaux, L., Labow, G. J., Witte, J. C., Thompson, A. M., Haffner, D. P., Kramarova, N. A., Frith, S. M.,
1165   Huang, L.-K., Jaross, G. R., Seftor, C. J., Deland, M. T., and Taylor, S. L.: Trends in global tropospheric
1166   ozone inferred from a composite record of TOMS/OMI/MLS/OMPS satellite measurements and the
1167   MERRA-2 GMI simulation, Atmospheric Chemistry and Physics, 19, 3257-3269, 10.5194/acp-19-
1168   3257-2019, 2019.
1169